



Double Bunch FEL at LCLS-II

LCLS-II-TN-20-09

(Jan. 2021, R1.1)

A. Halavanau, G. Zhou, C. Emma, A. Lutman, Y. Ding, A. Aquila, A. Krasnykh,
D. C. Nguyen, V. Aldaba, T. Montagne, F.-J. Decker, C. Mayes, D. Zhu,
S. Meuren, D. Reis, Z. Huang, A. Marinelli, S. Glenzer, C. Pellegrini
(SLAC National Accelerator Laboratory)

D. Cocco
(Lawrence Berkeley National Laboratory)

U. Bergmann
(University of Wisconsin, Madison)



Fermilab

Jefferson Lab

Contents

1	Purpose and Scope	3
2	Introduction	4
3	Start-to-end XFEL simulations	6
3.1	LCLS injector and copper linac performance	6
3.1.1	Beam propagation to the undulator entrance	8
3.1.2	Wakefield effects in the copper linac	8
3.2	FEL performance	10
3.2.1	Beam properties and matching	10
3.2.2	DBFEL at 4 keV	11
3.2.3	DBFEL at 7 keV	14
3.2.4	Comparison with ideal beam simulations	19
3.2.5	Comparison with existing HXR self-seeding	20
3.2.6	Superconducting and strong focusing undulators	21
4	Four bounce monochromator design	21
5	Double- and multi-bunch infrastructure	27
5.1	Double bunch jitter	28
5.2	Photoinjector IR pulse stacking	28
5.3	Ultra-fast e-beam kicker design	31
6	DBFEL scientific applications	33
6.1	2-photon absorption at 4 keV	34
6.2	High fluence diffractive imaging	35
6.3	DBFEL pump-probe two color mode	35
6.3.1	S-XES spectroscopy with two-bunch two-color operation	36
6.3.2	Coherent anti-Stokes Raman spectroscopy at 4 keV	37
6.4	Hard X-ray harmonic lasing	38
6.5	High Field QED: $e\gamma$ - and $\gamma\gamma$ -colliders	39

6.6	XFEL enhanced nuclear fusion cross-sections	42
-----	---	----

1 Purpose and Scope

This document describes the following aspects of the double bunch FEL (DBFEL) seeding concept at LCLS ¹:

- Electron beam preparation and orbital (trajectory) control, via start-to-end simulation analysis
- Ultra-fast electron beam kicker specifications and preliminary design
- Reflective four-bounce monochromator and X-ray delay line design
- LCLS photoinjector infrastructure upgrades, resulting in stable two- or four- pulses configuration
- Scientific applications of the DBFEL

When built, DBFEL will enable the following capabilities, previously inaccessible at LCLS:

- Very high power and brightness X-ray pulses, 200-300 GW, ten times the transmissive self-seeding brightness- in a tunable hard X-ray photon energy range of 4-7 keV. The pulses will be pre-pulse free and the configuration enables longer undulator tapering, contrary to the transmission self-seeding case
- With additional X-ray optics infrastructure, DBFEL can be used to study nonlinear atomic physics and strong field QED: a) the pulse can be focused to reach an electric field of 0.4 PV/m at 10 nm rms radius, well above the atomic electric field, in the lab system; b) backscattering the pulse on the FEL electron beam reach four times the Schwinger field; c) probe higher-order effects in photon-photon scattering (e.g. 2-loop Euler-Heisenberg process); d) serve as electron-photon and X-ray Gamma photon collider
- Two-color FEL pulses (pump-probe configuration) with two pulses tunable in photon energy and mutual separation

¹Work supported in part by the DOE Contract DE-AC02-76SF00515

- Reflective four-bounce monochromator for advanced FEL concept studies, e.g. harmonic lasing and superconductor undulator tests

2 Introduction

X-ray free electron lasers (XFELs) are a unique scientific instrument to explore nature at the Angstrom-femtosecond (fs) space and time scales. We propose here to further extend their capabilities by using the Double Bunch FEL (DBFEL) concept, an upgrade for the existing LCLS-II Hard X-ray (HXR) undulator beamline that enables fresh bunch seeding and results in about 10-fold improvement in X-ray power and brightness, as compared to regular HXR self-seeding operations. The proposed DBFEL at LCLS-II operates in the 4 to 7 keV photon energy range. In this scheme, shown in Fig. 1, the first bunch generates a high power, nearly saturated, SASE X-ray pulse in the first undulator section, and is not used in the second undulator section. The second bunch is seeded at the entrance of the second tapered undulator section by the monochromatized high power SASE pulse generated by the first bunch. The frequency filtering occurs in a four crystals monochromator, also acting as a photon delay line. A fast transverse kicker is used to put the second bunch in oscillations around the undulator axis in the first section to suppress the lasing process, while the first bunch is instead on axis. A magnetic chicane steers both electron bunches off the monochromator optics, and, at the same location, transverse orbit correctors are used to set the second bunch on axis in the second undulator tapered section, thus setting also the first bunch on an oscillating trajectory.

The DBFEL concept was first considered to improve the performance of the European XFEL and LCLS in Refs [1, 2, 3]. The overall design of the DBFEL at LCLS-II has been outlined in [4, 5]. A similar configuration using a second bunch as a fresh bunch with an ultra-fast kicker has been analyzed in the context of self-seeding and harmonic lasing in Ref. [6]. The experimental demonstration of fresh-slice self-seeding in a single bunch, a proof of principle of the DBFEL concept, was reported in Ref. [7].

The DBFEL requires a number of critical components to be added to a baseline XFEL beamline. First, two electron bunches must be produced in a photoinjector. In practice,

this is done by splitting the existing UV laser pulse into two pulses with a variable delay, or by using two synchronized cathode drive lasers. A second critical component is the four crystal Bragg monochromator, which filters the wide-band SASE X-ray pulse created in the first undulator section by the first electron bunch, providing the narrow-bandwidth radiation for seeding, and delays the radiation to coincide with the second electron bunch. The monochromator must be compact enough to fit inside the space of an undulator segment while sharing this space with other existing devices. These constraints dictate the maximal two bunch delay time. Both bunches must be properly controlled in the linac and undulators, to alleviate wakefield effects, to put the second bunch initially off-axis in the SASE section, and to return it back on-axis in the amplifier section. The setting of the trailing bunch

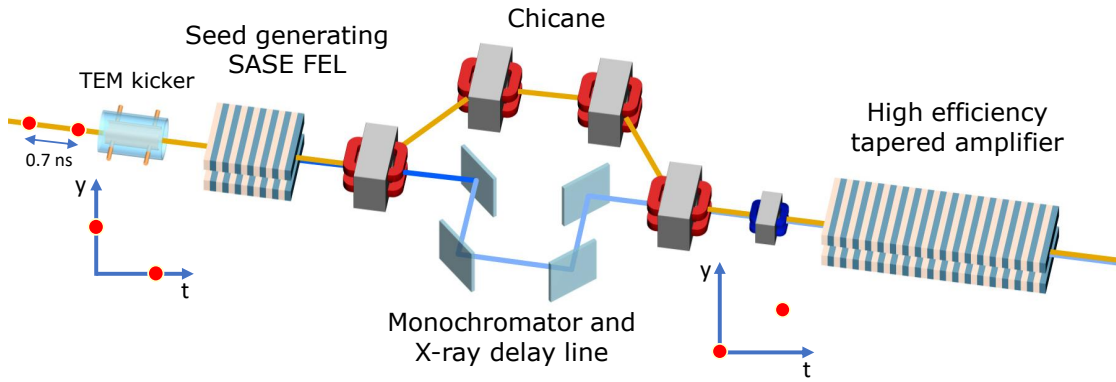


Figure 1: DBFEL schematics: Two bunches with 0.7 ns separation are produced in the injector, accelerated and compressed in the copper Linac, propagating co-axially to the HXR undulator sections. At the TEM kicker location, the second bunch is kicked off axis, while the first bunch propagates on axis generating a SASE X-ray pulse. The 4-bounce monochromator filters and delays the SASE X-ray pulse by 0.7 ns. The magnetic chicane steers the electrons off the monochromator optics creating a small delay of the electrons (some tens of fs). At the entrance to the second undulator section, the second bunch trajectory is steered back to propagate on axis. This bunch is co-aligned and temporally overlapped with the filtered and delayed x-ray pulse that acts as a monochromatic seed, while the first bunch is kicked off axis. The position of the monochromator in the chicane is presented separately in Fig. 20. Illustrations are not to scale.

off-axis is planned to be done by using an ultrafast transmission line kicker with a rise time of 0.5 ns.

This note is organized as follows. We first discuss the DBFEL performance using start-to-end numerical simulations and define the photon energy range of operation. We then describe the design of the DBFEL X-ray monochromator and ultra-fast kicker. Finally, we discuss several scientific research opportunities enabled by DBFEL in high-field atomic physics and QED, X-ray spectroscopy, accelerator-, FEL- and fundamental physics.

3 Start-to-end XFEL simulations

A detailed numerical study of the DBFEL performance based on a range of assumed electron beam parameters was done in our recent paper [4]. Here we report a summary of results obtained using start-to-end simulations to obtain more realistic performance characteristics. The simulations are done in three steps. We first consider the LCLS copper linac injector using the code IMPACT-T [8]. The beam is then passed to the particle tracking program ELEGANT [9] and propagated to the entrance of the HXR undulator (schematically shown in Fig. 2). This process is streamlined, allowing for future optimization of LCLS HXR beamline. The particle distribution at the undulator entrance is then converted and passed to the FEL code GENESIS [10] wrapped into a Python package for analysis and tapering optimization [11]. In this process we have to consider the difference between the first and the second bunch propagating through the injector linac and undulator. The main difference between the two is the effect of the wakefields generated by the first bunch and acting on the second bunch. We analyze this effect and show that by a proper choice of the separation between the two bunches it can be minimized and controlled such, that the properties of the first and second bunch are similar enough to justify using the same GENESIS results.

3.1 LCLS injector and copper linac performance

The performance of the LCLS copper linac injector is evaluated using the beam physics code IMPACT-T and a package LUME-IMPACT [12] to change parameters and optimize the electron beam. The optimization is done changing the injector solenoid field amplitude, RF voltages

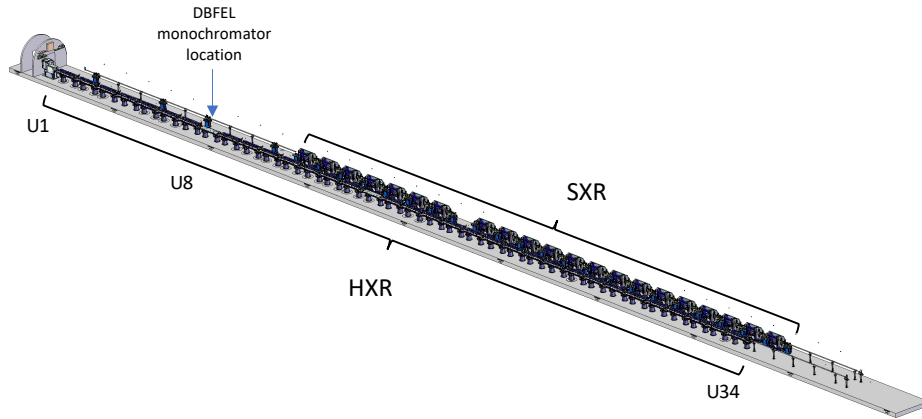


Figure 2: LCLS-II undulator hall schematics.

and phases of the L0A/B linacs and injector quadrupoles strength to match the injector beam into the LCLS copper linac. The beam parameters assumed for the calculation and the resulting emittance and energy spread are shown in Tab. 1. The beam phase space plots near the injector exit are shown in Fig. 3. We note that L0B phases must be put -5.5 degrees off-crest to minimize final injector energy spread.

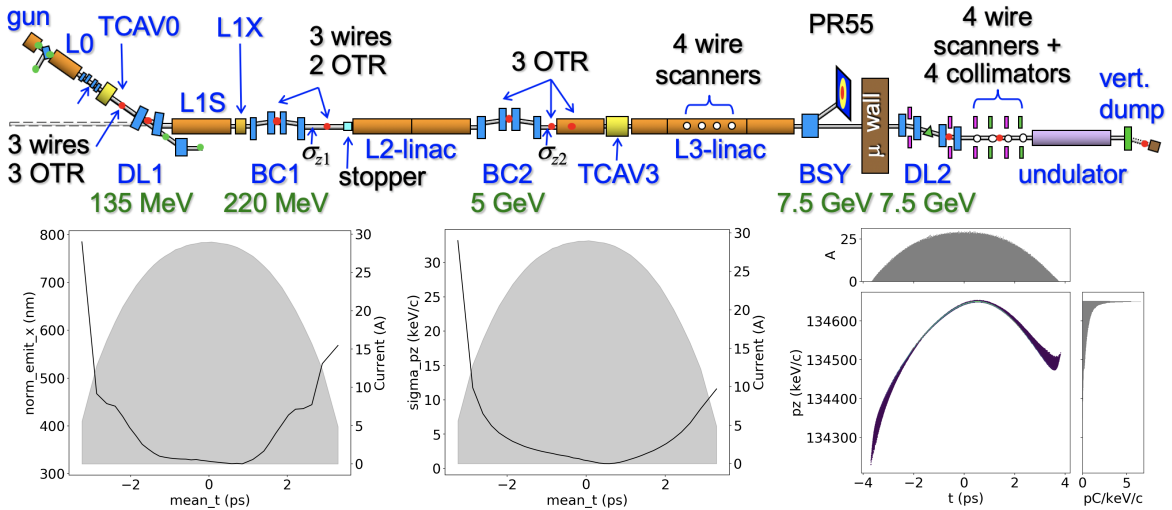


Figure 3: LCLS copper linac layout schematics and e-beam properties at OTR2 location (before DL1) of the LCLS copper linac injector.

Parameter	Units	Value
Electron bunch charge, Q	pC	250
Spot size at the cathode, σ	mm	1.2
Number of macroparticles, N	10^6	10
OTR2 normalized slice, ϵ_x	μm	0.295
OTR2 normalized slice, ϵ_y	μm	0.271
OTR2 slice energy spread, σ_{pz}	MeV/c	1.2
BC1 collimator full-width	mm	6.6
Laser heater setting	keV	21

Table 1: Start-to-end beam dynamics simulation parameters. The number of macroparticles is that used in the simulations.

3.1.1 Beam propagation to the undulator entrance

The beam simulated in the photoinjector is accelerated through the copper linac and propagated to the HXR undulator entrance, using beam dynamics code ELEGANT, including effects like coherent synchrotron radiation. Figure 4 shows the longitudinal phase space, the emittance and energy spread at the undulator entrance for the case of 6.6 GeV final beam energy, corresponding to 4 keV photon energy. The beam core peak current, and energy spread are about 3.6 kA, 1.7-2.5 MeV. The beam head has lower energy spread than the tail. The normalized emittance in x and y planes is about $0.4 \mu\text{m}$. Similar plots are obtained when accelerating the beam to 9.25 GeV to obtain 7 keV photon energy. These distributions are used as an input to GENESIS to evaluate the FEL performance.

3.1.2 Wakefield effects in the copper linac

In general, the second bunch is subject to multiple longitudinal and transverse wakefields introduced by the first bunch, particularly in the copper linac structure. The effect of the longitudinal wakefield (energy loss) can be compensated by tuning the phase of the laser at the photocathode [13, 4]. Transverse wakefield in the leading order can be calculated by

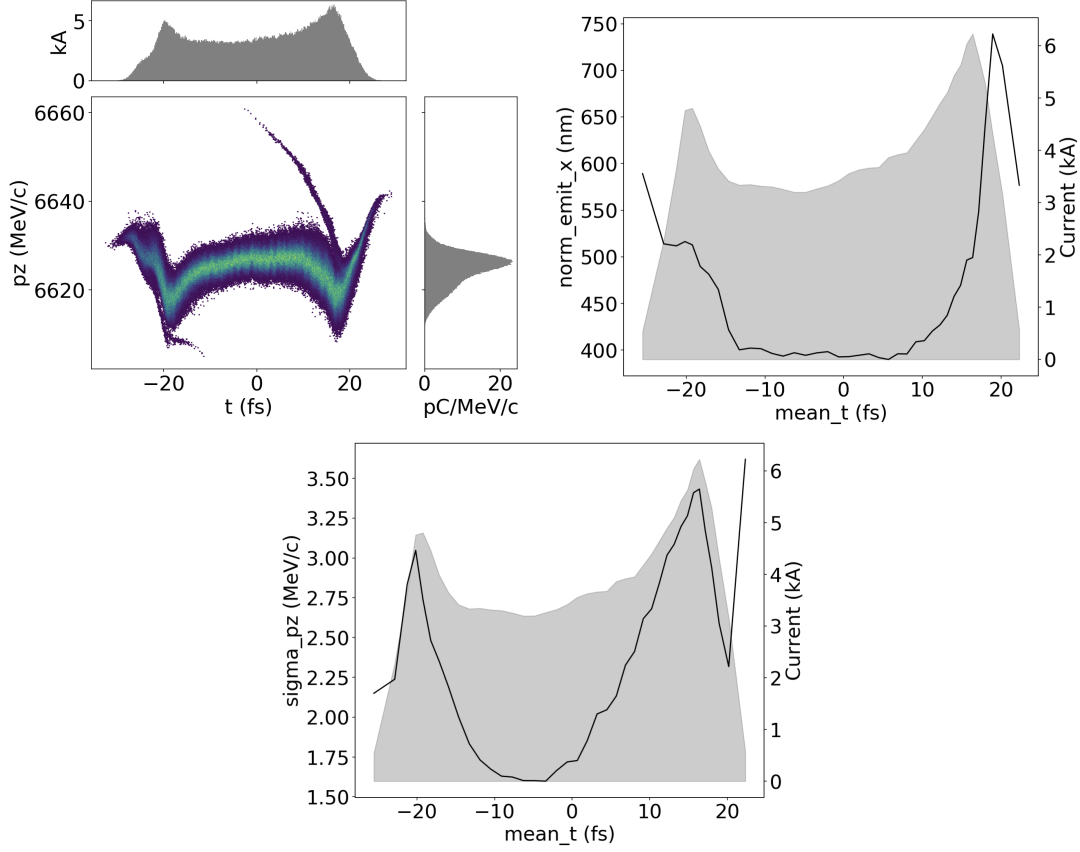


Figure 4: Top row: Longitudinal phase-space (LPS) of 4 kA, 6 GeV beam at the HXR undulator entrance (left) and normalized transverse slice emittance (right). Bottom plot: slice energy spread. The gray shade area depicts the beam current profile.

using the expression [14]:

$$W_y(t) = \sum_n 2\kappa_{y1n} \sin(2\pi f_{1n}t) e^{-\pi f_{1n}t/Q_{1n}}, \quad (1)$$

where f_{1n} and κ_{y1n} are the modes' frequencies and kick parameters respectively, and $Q_{1n} \approx 18000$. A plot of the long-range transverse wakefield kick is shown in Fig. 4.

Figure 5 shows that for two RF-buckets corresponding to 0.7 ns separation between the two bunches the long range transverse wakefield effects are minimized. The next datapoint - 3 RF-buckets or 1.05 ns separation - yields 1 μ rad transverse slope of the second bunch induced by a maximum transverse displacement of the first bunch of 0.1 mm. Left uncorrected, with a betatron function of 20 m, it yields 20 μ m maximum displacement, comparable to the RMS spotsize of the second bunch. However, since only one bunch needs to be on-axis per

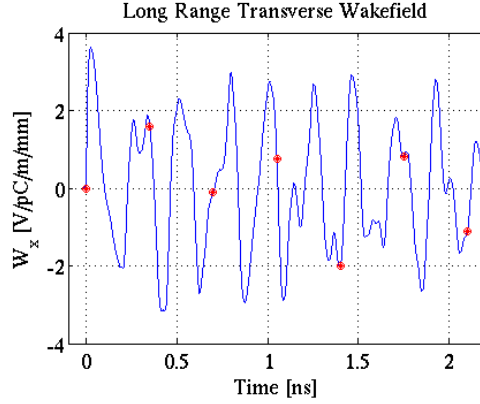


Figure 5: Long range wakefield in LCLS copper S-band linac acceleration cavities as a function of bunch separation

undulator section, the displacement can be compensated with dipole correctors, similarly to the split undulator scheme [7]. To minimize detrimental effects of the long range wakefields in the copper linac, we consider in the following the case of two RF-bucket i.e. 0.7 ns separation between bunches.

3.2 FEL performance

In this section, we investigate the performance of DBFEL using the code GENESIS and undulator tapering, using the approach similar to that of references [4, 5, 15]. The results show that with a selected taper profile the DBFEL can generate a narrow bandwidth pulse with a power more than 300 GW at 4 keV photon energy and more than 200 GW at 7 keV. It is worth mentioning that with further optimization on the monochromator and taper profile, it is possible to achieve higher power in the future [16, 17, 18].

3.2.1 Beam properties and matching

The properties of the core part of the e-beam (about 15 fs long), used as an input in GENESIS, are shown in Fig. 4. As one can see in Fig. 6, the core part of the electron beam is well matched at the start of the undulator and the beam size oscillates along the undulator with an rms beam radius of about 10 μm .

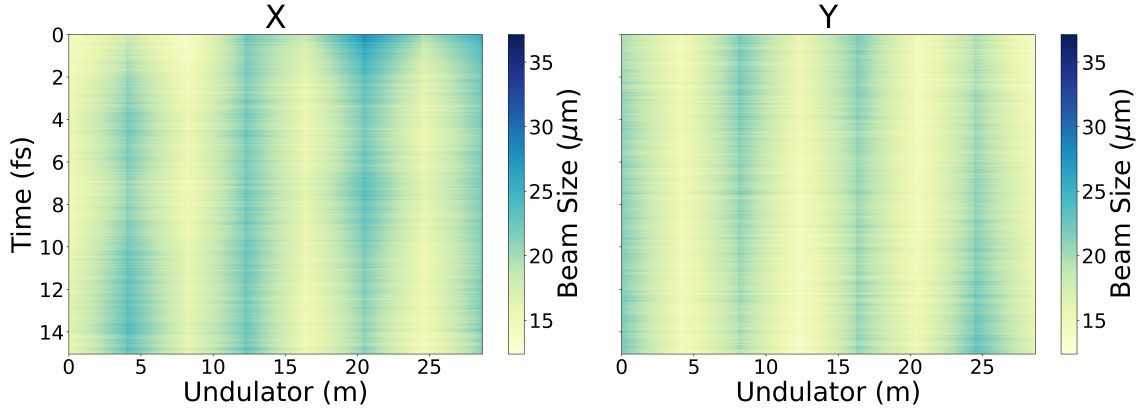


Figure 6: Electron beam size evolution in the SASE section (seed generator) of the undulator line in x (left) and y (right) direction.

3.2.2 DBFEL at 4 keV

We first consider DBFEL operation at 4 keV photon energy, which is close to the lower limit of hard X-ray self-seeding scheme. Figs. 7, 8 show the properties of the SASE stage of DBFEL: average power (Fig. 7, left), beam current (Fig. 7, right), temporal power profile (Fig. 8, right) and the power spectrum (Fig. 8, left). The calculations are done for 256 random noise SASE cases to evaluate the fluctuation in the final output X-ray properties. The multi-shot average presented in Fig. 8 and the beam current profile in Fig. 7 are well correlated.

The four-bounce monochromator filters the SASE signal and produces a seed for the tapered amplifier section. As shown in Fig. 9, we observe strong shot-to-shot fluctuations due to the combination of the narrow monochromator bandwidth, 6×10^{-5} , and the spiky nature of the SASE seed signal. This is the dominant source of fluctuations in the final output power. The maximum attainable seed power is about 100 MW. The histogram of the seed power is shown in Fig. 10 (left) showing an average seed power of approximately 14 MW. As shown in Fig. 9, the seed signal generated by a four-bounce monochromator has much better longitudinal coherence properties compared with that of a SASE pulse, [19].

With taper optimization on both power and bandwidth, we obtain a taper profile and its corresponding FEL gain curve, shown in Fig. 11. The spectral profiles of the 4 keV

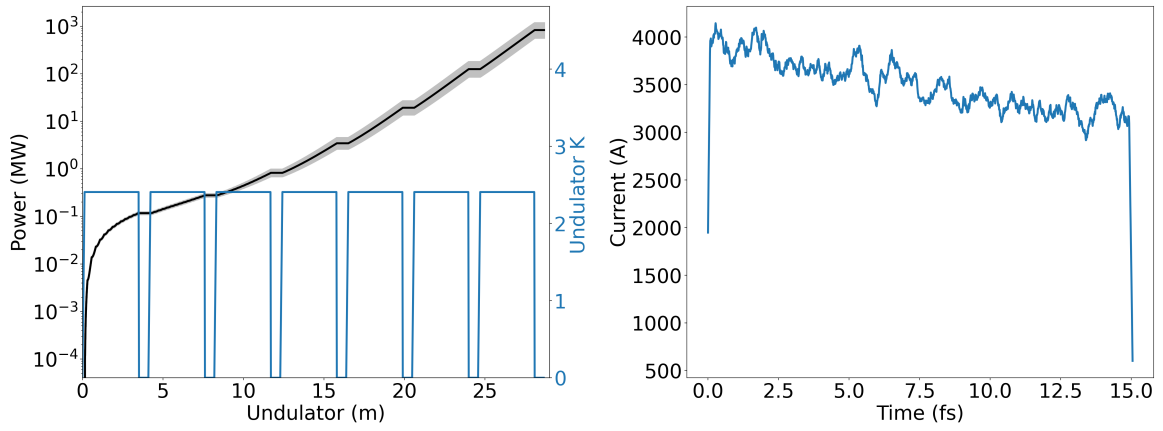


Figure 7: DBFEL performance at 4 keV in the SASE section: FEL power (left), gray lines represent shot-to-shot performance and the black curve is a multi-shot average; temporal profile (right) at the SASE section exit.

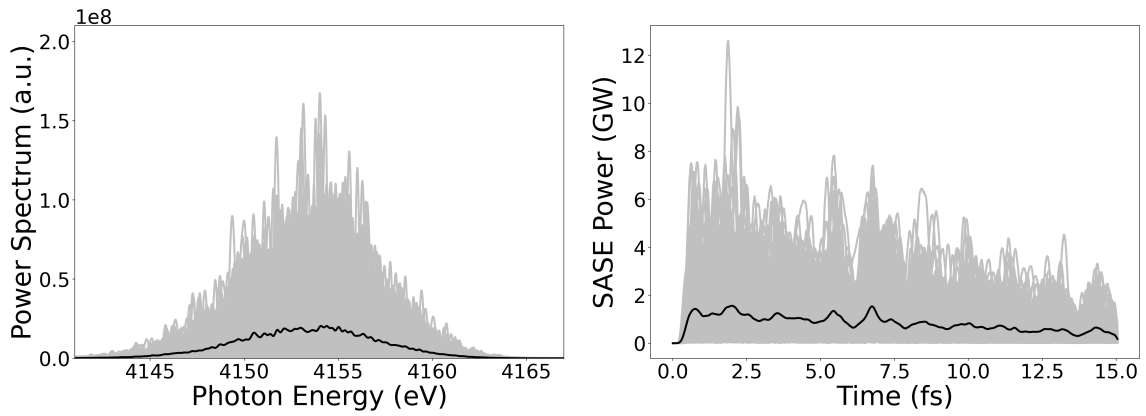


Figure 8: DBFEL performance at 4 keV at the SASE section exit: FEL power spectrum (left) and temporal profile after the SASE section (right). Gray lines represent shot-to-shot performance and the black curve is a multi-shot average.

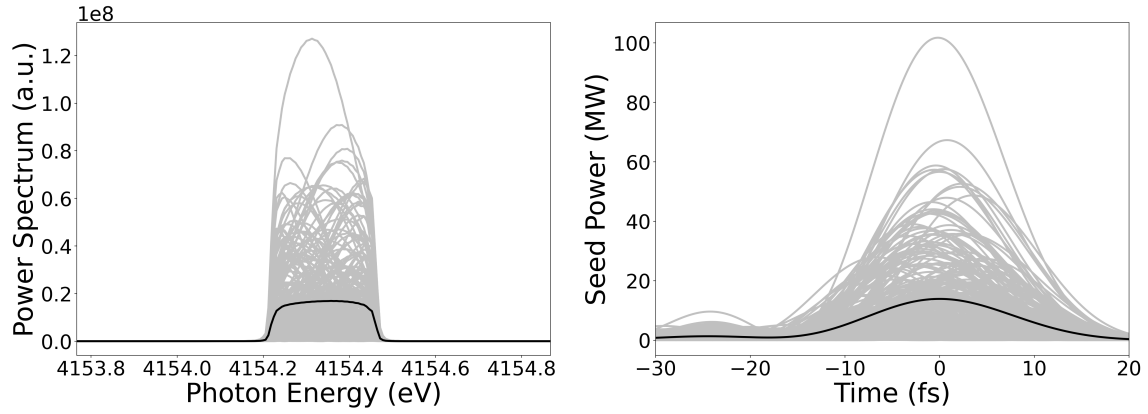


Figure 9: Seed pulse parameters after four-bounce $C^*(111)$ monochromator: spectral (left) and temporal (right) profiles. Gray lines represent shot-to-shot performance and the black curve is a multi-shot average.

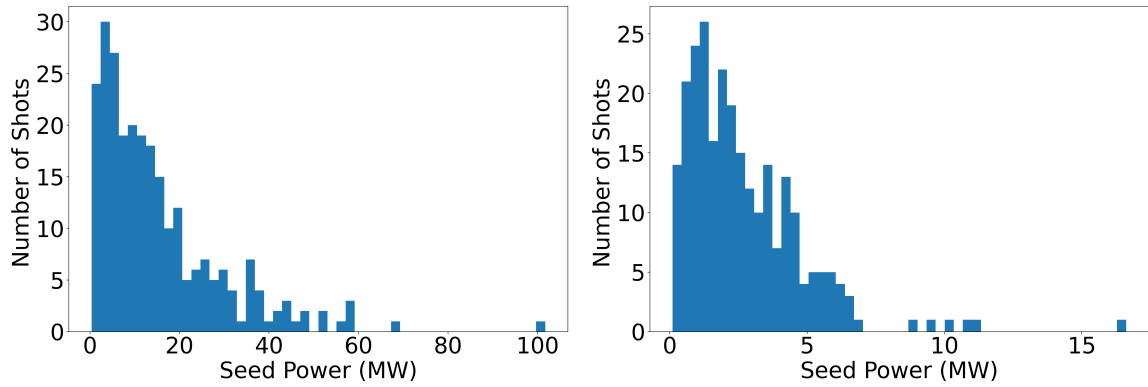


Figure 10: Statistical performance of DBFEL seed power: power histogram of 4 keV (left) and 7 keV (right) pulses.

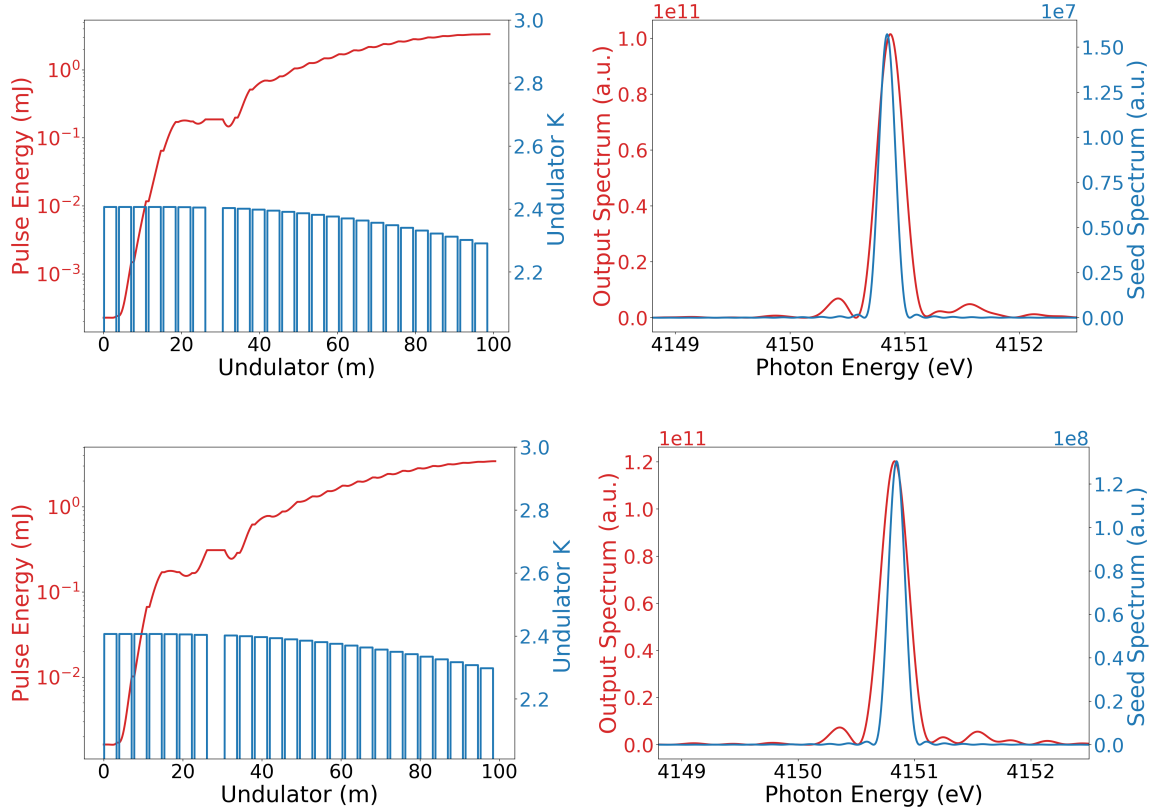


Figure 11: The performance of DBFEL operating at 4 keV photon energy. Tapering profile and corresponding gain curve (left) and pulse spectrum (right) for average (top) and peak (bottom) performance. Detailed quantitative description can be found in Table 2.

pulse at the amplifier exit are shown in Fig. 11 for two cases corresponding to the maximum seed power, 101 MW (bottom row), and the average seed power, 14 MW (top row). The temporal profile of the output pulse with the best seed can be found in Fig. 12. The power and bandwidth values at the undulator exit for the two cases are given in Table 2. Notice that the difference in output power between the two cases is only about 15%. The final output FEL signal has a bandwidth slightly larger than that of the monochromator seed signal.

3.2.3 DBFEL at 7 keV

Here, we present 7 keV SASE pulse performance in in Figs. 13 and Fig. 14. The correlation between the multi-shot average in Fig. 14 and the electron beam current profile in Fig. 13

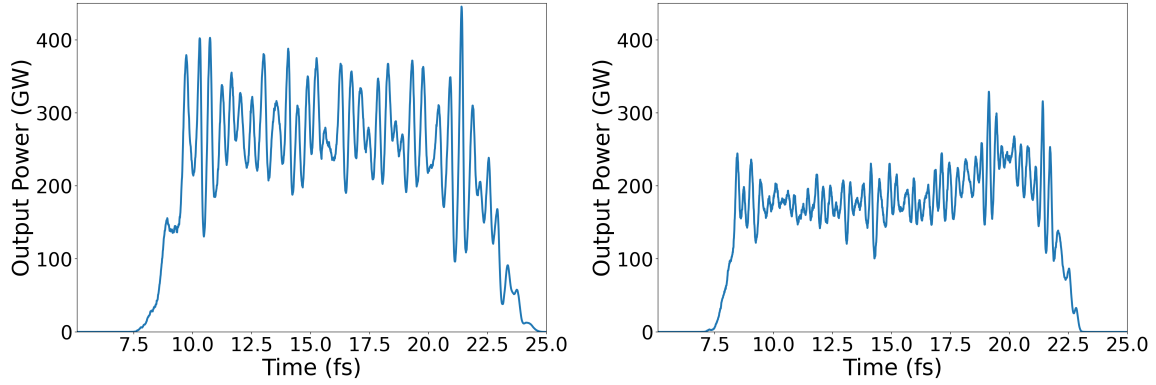


Figure 12: The temporal profile of DBFEL output pulse: 4 keV case (left) and 7 keV case (right).

can be observed.

Similar to the 4 keV case, the four-bounce monochromator has been employed to filter the SASE signal and produces a seed for the tapered amplifier section. The temporal and spectral profiles of the 7 keV seed can be found in Fig. 15. In Fig. 15 the seed signal displays, again, strong fluctuations. The maximum attainable power is about 20 MW, which is about 1/5 of the 4 keV case. The histogram of the seed power is shown in Fig. 10 (right), according to which, the average seed power is around 2 MW.

Again, with a careful optimization on both power and bandwidth, we obtain a taper profile and its corresponding FEL gain curve, shown in Fig. 16. The spectral profiles of the 7 keV pulse at the amplifier exit are shown in Fig. 16 for two cases corresponding to the maximum seed power, 20 MW (bottom row) and the average seed power, 2 MW (top row). The temporal profile of the output pulse with the maximum seed can be found in Fig. 12. The power and bandwidth values at the undulator exit for the two cases are given in Table 2. Similarly, the difference in output power between the two cases is only about 13% and the final output FEL signal has a bandwidth slightly larger than that of the monochromator seed signal.

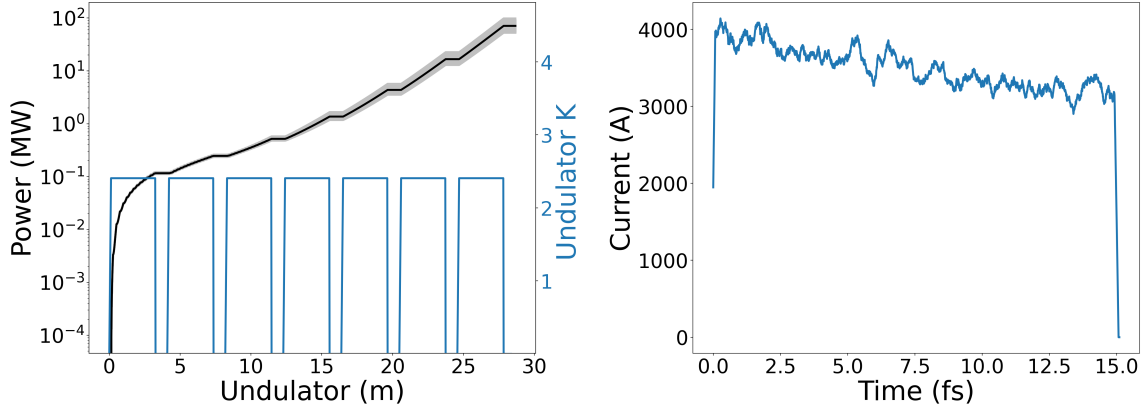


Figure 13: DBFEL performance at 7 keV in the SASE section: FEL power (left), gray lines represent shot-to-shot performance and the black curve is a multi-shot average; temporal profile (right) at the SASE section exit. .

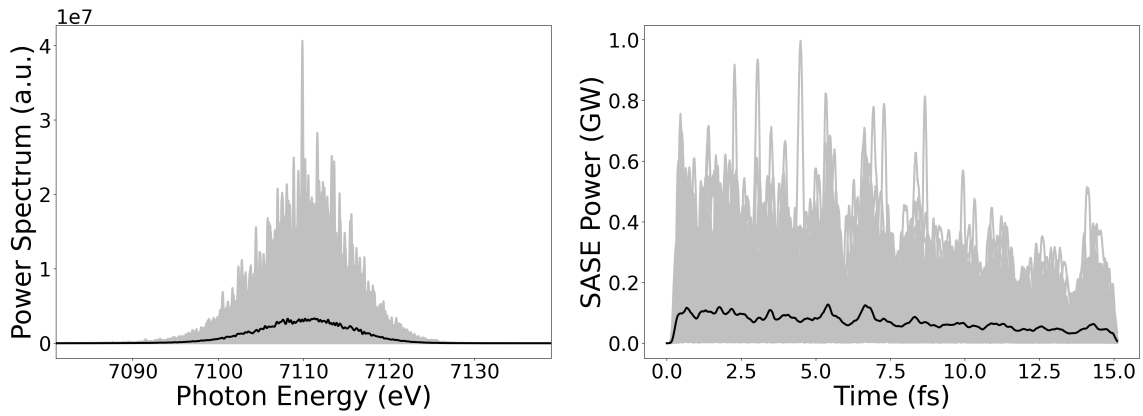


Figure 14: DBFEL performance at 7 keV at the SASE section exit: FEL power spectrum (left) and temporal profile after the SASE section (right). Gray lines represent shot-to-shot performance and the black curve is a multi-shot average.

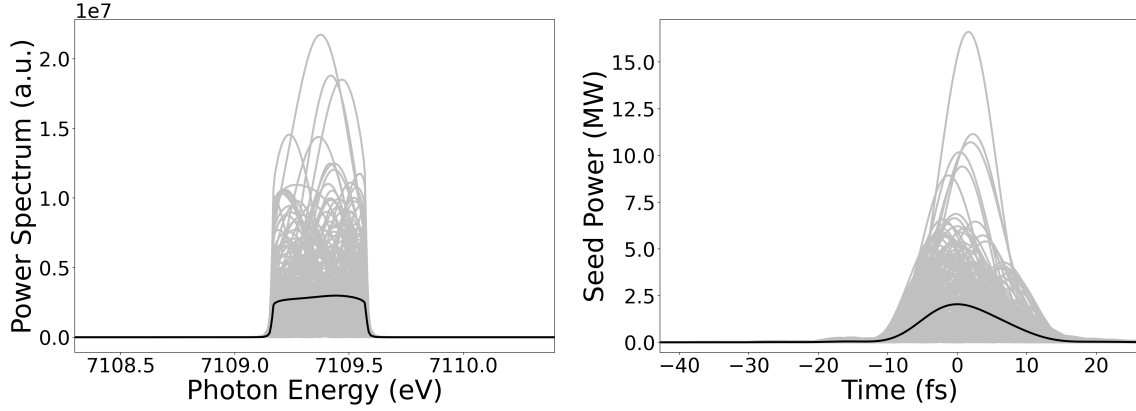


Figure 15: Seed pulse parameters at 7 keV after four-bounce $C^*(111)$ monochromator: spectrum (left) and temporal profile (right). Gray lines represent shot-to-shot performance and the black curve is a multi-shot average.

	4 keV	7 keV	Units
Pulse duration	15	15	fs
Ave. seed power	14.2	2.01	MW
Max seed power	101.6	16.4	MW
Ave. output power	257	150	GW
Max output power	301	212	GW
Ave. output pulse energy	2.97	2.10	mJ
Max. output pulse energy	3.44	2.45	mJ
FWHM of Ave. case	6.71×10^{-5}	3.73×10^{-5}	a.u.
FWHM of Max. case	6.56×10^{-5}	3.89×10^{-5}	a.u.

Table 2: Summary of start-to-end simulations

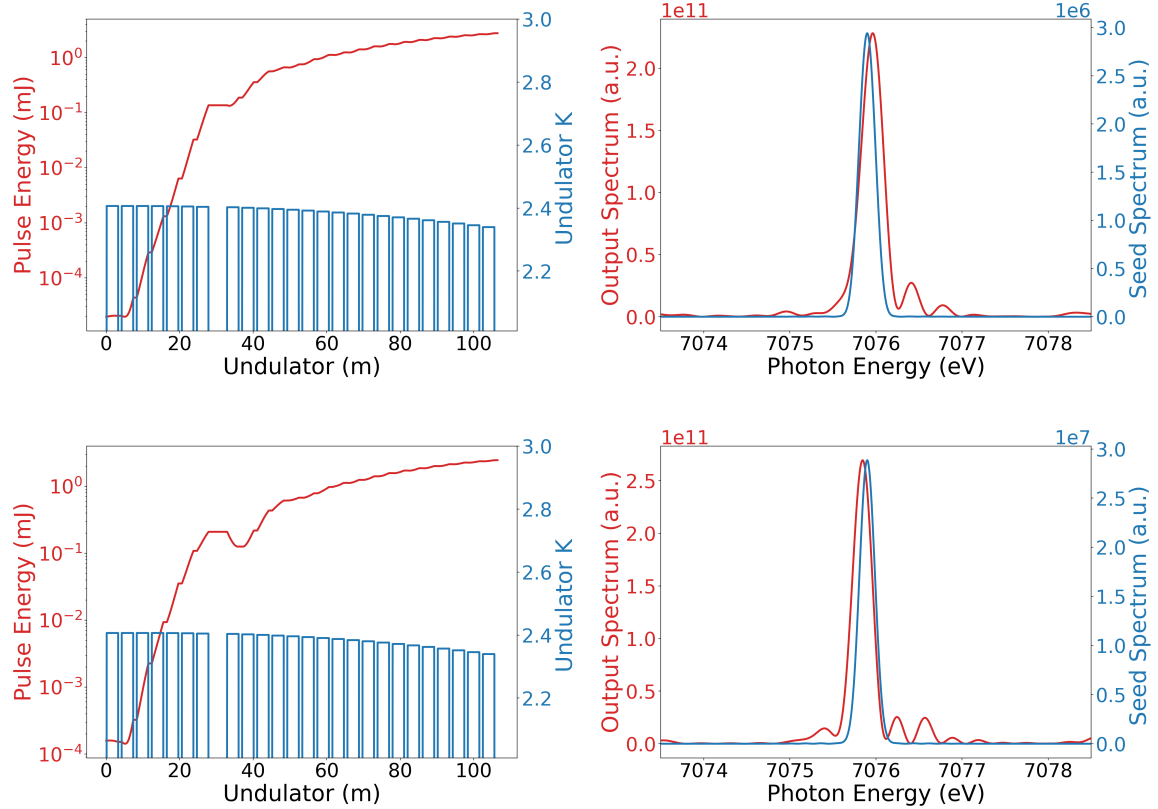


Figure 16: Performance of DBFEL operating at 7 keV photon energy. Tapering profile and corresponding gain curve (left) and pulse spectrum (right) for average (top) and peak (bottom) performance. Detailed quantitative description can be found in Table 2.

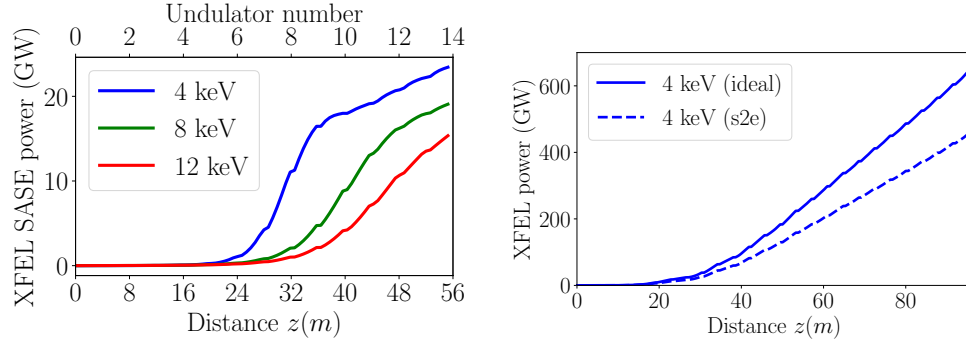


Figure 17: Left: Start-to-end beam performance in the SASE section XFEL power as a function of distance for different photon energies. Right: An example of projected tapered undulator section performance at 4 keV, when locating the monochromator after seven undulator sections.

3.2.4 Comparison with ideal beam simulations

In Ref. [4] we evaluated the performance of DBFEL, using the HXR undulator of LCLS and the copper linac, using ideal beam parameters consistent with the normal LCLS operation. Figure 17 displays the FEL power curves for different photon energies in the SASE section at two possible points for the monochromator insertion at the position of undulator sections 8 and 15, using start-to-end simulations for the beam described above. 4 keV case saturates after 8 undulators. At the next empty slot at U15 SASE pulses with photons between 4 keV and 8 keV are saturated. A SASE section of 7 undulators results in more power for DBFEL than 14 undulators, since the amplifier section in the first case is longer. We note, that ultimately, experimental electron beam parameters and hard X-ray gain length should be the key factors that determine the location of the DBFEL four crystal monochromator. These measurements are planned shortly after LCLS-II HXR undulator commissioning. In this document, however, we will consider the baseline design of the LCLS-II HXR undulator with the DBFEL monochromator installed in section U8.

After propagating an *ideal beam* through the SASE section (first 7 LCLS-II HXR undulators), the maximum SASE power for 4 keV photons is about 6 GW. It is then reduced to about 150 MW after the $C^*(111)$ monochromator, delayed and overlapped with the second

bunch. Fig. 17 illustrates the XFEL power as a function of distance in the LCLS-II HXR undulator for 4 keV photons. We point out that it is just one possible way of tapering, and there are possible future detailed optimizations of this scheme, yielding better results. However, even with selected tapering strategy, we demonstrate a substantial improvement over maximum XFEL power ever obtained at LCLS [20].

3.2.5 Comparison with existing HXR self-seeding

Currently, LCLS-II HXR beamline employs a transmission self-seeding system, with a thin diamond crystal located inside a chicane at U16 location. Due to transmission mode, this system operates mostly at hard X-ray range, to mitigate absorption effects in the crystal.

Here, we investigated the performance difference between conventional transmissive self-seeding and the DBFEL scheme. Using the same diamond atomic layer to filter the first section SASE signal to generate the narrow bandwidth seed, after the second stage amplification, the final output signal comparison is shown in Fig. 18. As it is shown there, both for 4 keV and 7 keV case, the DBFEL scheme has about ten times more photons in the central spectral line and ten times higher brightness, since it has 7 more undulator sections for tapering and a brighter seed. Also, as we can see in Fig. 18, DBFEL has better signal-noise ratio compared with transmissive self-seeding.

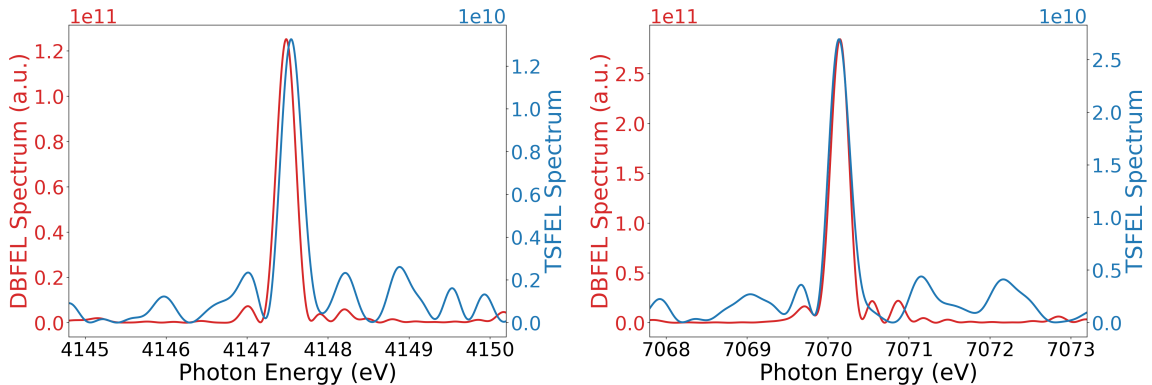


Figure 18: Power spectrum comparison between DBFEL and transmissive self-seeding FEL (TSFEL): photon energy at 4 keV (left) and 7 keV (right).

3.2.6 Superconducting and strong focusing undulators

Superconducting planar/helical undulators with distributed transverse focusing can be used to increase the XFEL power extracted from the electron beam in the amplifier section, . This concept, referred to as Advanced Gradient Undulator (AGU), was investigated in [21]. We have done a preliminary estimates of the peak power obtainable using the same seed values as used in our start-to-end simulations, and an ideal beam to evaluate the amplification in a superconducting AGU undulator about 100 m long, with the same parameters used in Ref. [21]. The results show that multi-terawatt 12 keV photon pulses can be generated, as seen in Fig. 19. Similar conclusions have been drawn in a normal conducting undulator with a very strong focusing FODO lattice [22].

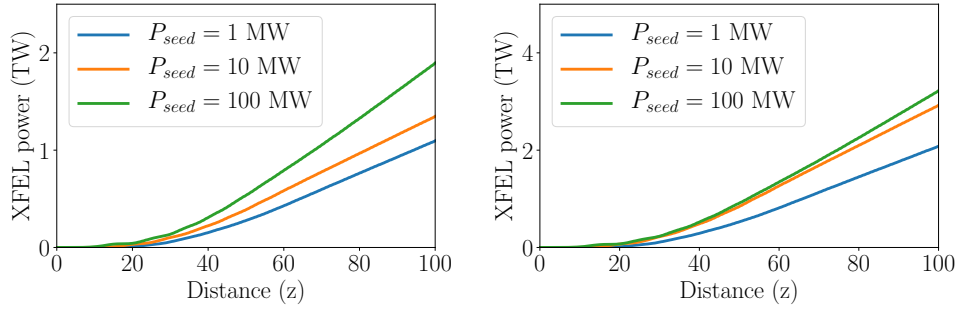


Figure 19: Tapered 100 m planar AGU (left) and helical AGU (right) XFEL peak power at 12 keV with different seed power values.

4 Four bounce monochromator design

A four-bounce system offers high seed power due to the high reflectivity of the crystals, narrow bandwidth and tunability over large photon energy range. A similar scanning four-bounce monochromator at the Diamond Light Source (DLS) facility has been successfully implemented and commissioned [23]. The delay in the monochromator matches the delay $\Delta\tau$ between the two bunches. In order to proceed with the design of the four bounce monochromator, let us discuss a few salient parameters of this device. We first start with the location of the monochromator in the undulator beamline. LCLS-II HXR undulator has

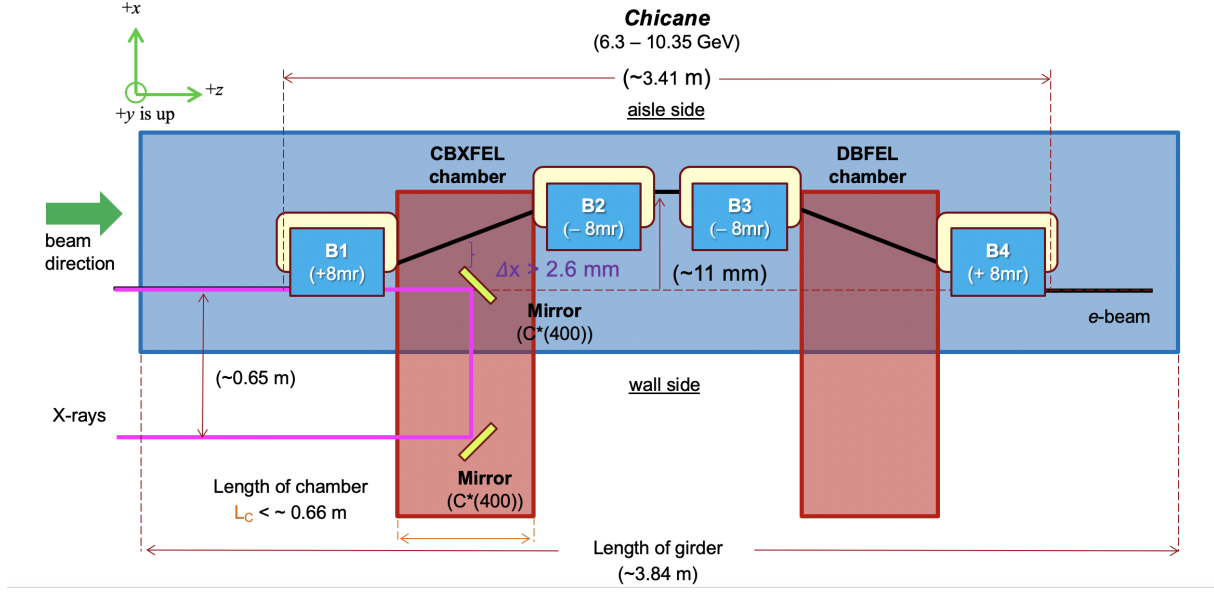


Figure 20: DBFEL four crystal monochromator location in the magnetic chicane. A space suitable for installation of DBFEL monochromator is available between the third and the fourth chicane magnet. See Ref. [24] for the description of the CBXFEL project.

34 girders with 32 undulator segments (U1-U34), each 3.6 m long, separated by a 1.0 m of free space; see Fig. 2. Two empty slots at U8 and U15 are available for installation. The DBFEL monochromator is planned to be installed in the same chicane with the proposed LCLS-II CBXFEL project (see Fig. 20) in the slot U8, limiting its horizontal size to $L = 0.67$ cm. Currently, slot U15 is scheduled for HXRSS installation, with a single thin diamond crystal operating in the forward Bragg diffraction (transmission) mode. To accommodate both optical systems (CBXFEL and DBFEL) in the same chicane, we consider an XLEAP style chicane, with two inner magnets pushed very close to each other, while maximizing two empty spaces. In this configuration, the chicane magnets provide a >3 mm clearance for the diamond optics in DBFEL monochromator for the operating beam energy range of 6-8 GeV.

The monochromator uses diamond crystals to provide a narrow bandwidth and avoid complex thermal management [4]. We chose C*(111) diamond crystals as the best option for 4-7 keV energy range. C*(111) parameters are given in Tab. 3. The monochromator bandwidth is determined by the Darwin width, which is plotted in Fig. 21. Darwin curves were produced in XOP program [25].

Parameter	Units	Value (4 keV)	Value (7 keV)
Bragg angle	deg.	48.8	25.5
Darwin width	μrad	69.4	28.6
Extinction length	μm	2.9	5.0
Bandwidth	$\cdot 10^{-5}$	6.1	6.1

Table 3: C*(111) parameters in 4-7 keV photon energy range.

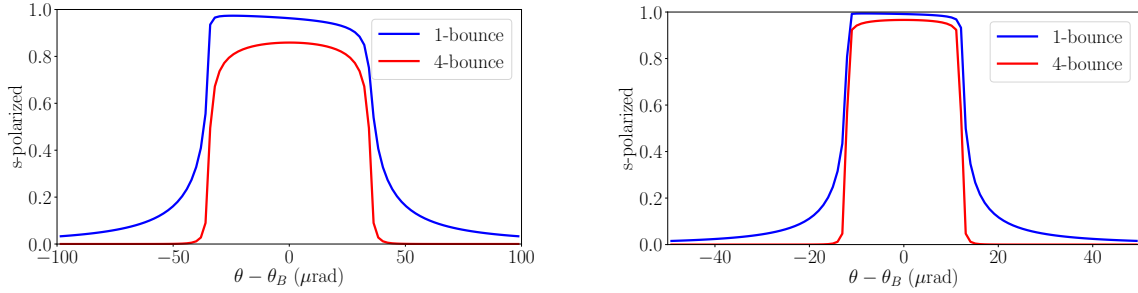


Figure 21: Darwin width of C*(111) 4 keV (left) and 7 keV (right) reflections for single and four bounces.

The choice of diamond reflection also defines the geometry of the monochromator via the value of Bragg angle θ . Simple kinematic calculations yield the following equations for monochromator crystals' coordinates. Let us denote the distance between the two upper crystals by L . Then the separation between two lower crystals is determined by

$$\Delta_z = L - c\Delta\tau(\cot^2 \theta - 1)/2 \quad (2)$$

and the lateral displacement by $h = c\Delta\tau/2 \tan \theta$. In addition, the bandwidth is defined by

$$\Delta\omega/\omega = -\Delta\theta/\tan \theta, \quad (3)$$

where $\Delta\theta$ is the Darwin width. Thus, driven by the space limitations and four crystal geometry, we determine the photon energy range for two bunch separation $\Delta\tau=0.7$ ns to be 4-7 keV. This calculation is summarized in Fig. 22. The delay of 1.05 ns is also possible, however it will require a different chicane design, incompatible with CBXFEL project.

Alternatively, one can consider the next diamond Bragg reflection of C*(220) to operate at higher photon energies, e.g. up to 12 keV, while reducing the footprint of the monochromator.

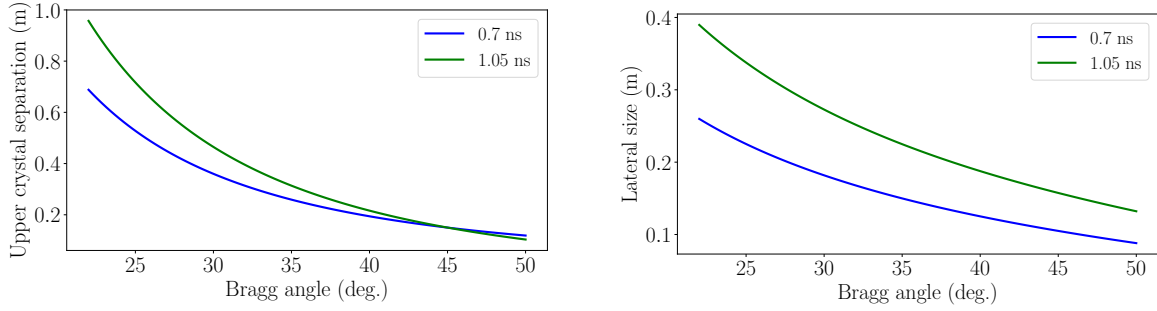


Figure 22: Four crystal monochromator size as a function of Bragg angle for 2 and 3 RF buckets double bunch separation and $\Delta z = 0.15$ m.

However, to primarily access 4 keV photons, we consider C*(111) as our primary choice. C*(111) will be procured from Sumitomo Electric and tested at Spring-8 facility in Japan. Type IIa single crystal HPHT diamonds are more resilient than Si to XFEL radiation damage, and provide better reflectivity than Si in the photon range of 4-8 keV. We also note the existing nanopositioning stages have a precision of about 20 nm, which translates into about ± 0.2 fs error in total delay time $\Delta\tau$. We estimate the effect of the angular pointing error via $\Delta\tau \sim \Delta\theta / \cos\theta^2$ to be of the order of 1 fs.

We then proceed to discuss mechanical design of the monochromator. Outside and inside views of the monochromator are displayed in Figs. 23, 24, 25. The design of the monochromator consists of a vacuum chamber supported by a strut system that is mounted directly onto the girder. The vacuum chamber will have a removable top lid with different types of ports welded on it. Two ports will be for vacuum hardware which are a set of gauges and valves and an ION pump. There will also be four small viewports for allowing cameras to detect the location of yag crystals at different yag locations inside the chamber. Two large viewports will also be on the top lid to allow for extra viewing.

The south wall of the vacuum chamber has two large viewing ports to allow for people to view the system and components locations inside. The side walls have one ConFlat flange each for connection to the bellows that are part of the beamline axis and rest of the beamline system. The north wall of the vacuum chamber has seven pin feedthroughs welded on that will allow for cabling connection from inside to outside the chamber to a controller for user operation. The entire system inside the chamber is supported by a kinematic stage that

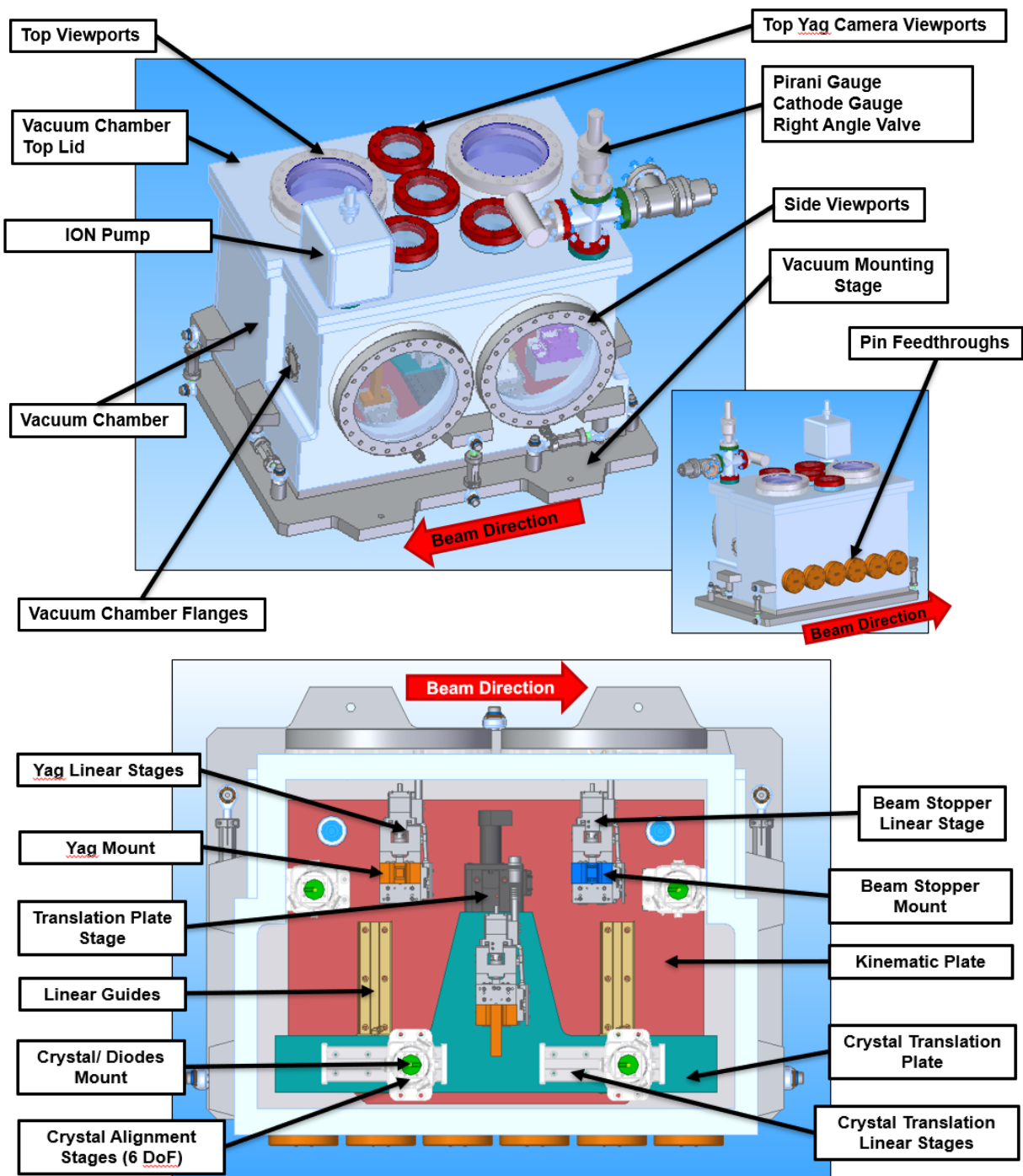


Figure 23: Four crystal monochromator chamber outside (top) and inside (bottom) view.

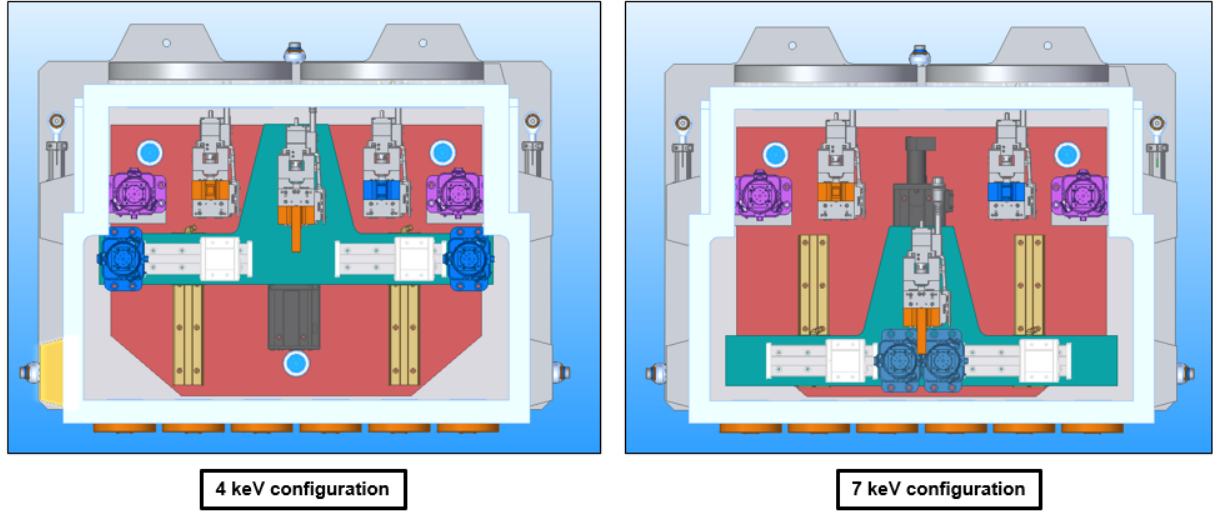


Figure 24: Four crystal monochromator (top view) in two configurations: 4 keV and 7 keV.

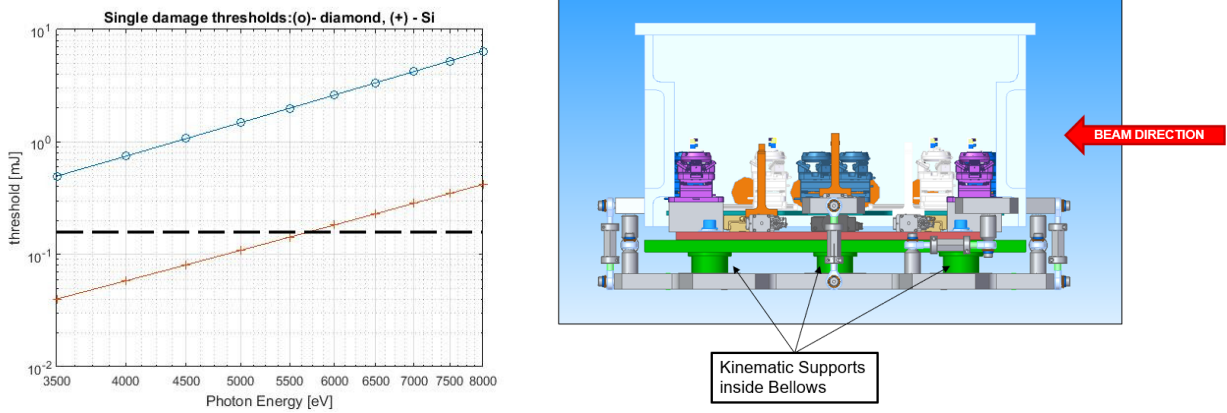


Figure 25: Thermal and mechanical stability of the monochromator: Instantaneous damage thresholds for C^* and Si crystals as a function of XFEL photon energy. Dashed line is expected SASE FEL performance (left). Illustration of the kinematic mounts of monochromator chamber. Kinematic plate, and therefore diamond optics, are attached directly to the girder for enhanced mechanical stability (right).

consists of three kinematic mounts and a plate that allows for leveling of the surface. The kinematic stage is used to minimize interference to the system from the vacuum chamber floor, which will deflect upwards once it is in vacuum. On top of the kinematic stage, there are four sets of diamond crystals that are each mounted on a six degrees of freedom (6DoF) stage that gives control for tunability. Two of these stages are in line with the beamline axis at different ends of the vacuum chamber where the connecting flanges are located. The other two stages are each mounted on linear stages that travels parallel to the beamline. These long range stages allow for the 6DoF stages to travel to a different position that will allow for a different energy configuration. The linear stages are also mounted on a plate that covers long range travel perpendicular to the beamline for maximum planar mobility. This plate is able to travel perpendicular to the beam line since it is attached to a linear stages that moves the same direction, and the plate is supported at the ends with linear guide rails that reduce vibration in the system. These guide rails and linear stage are directly mounted onto the kinematic stage. The 6DoF stages each hold a kinematic mount for the diamond crystal, as well as diodes that will move in and out of the path of the beamline as necessary to determine where the beam is and where to position the crystal accordingly. There are two YAG crystals mounted on linear stepper motor stages that will allow for determining beam position. One of the yag crystals is placed along the beamline axis. The other YAG crystal stage is mounted on the beamline perpendicular moving stage plate. This allows for the YAG crystal to move with the other two diamond crystal stages together, which allows for the YAG crystal to move in and out of the way of the beam between these two stages at different positions. There is another linear stepper motor stage along the beamline axis that is mounted on the kinematic plate that holds a beam stopper and is able to move in and out of the way of the beam.

5 Double- and multi-bunch infrastructure

Over the years of LCLS operations, electron beams containing multiple bunches separated by a few RF-buckets have been routinely created in LCLS copper linac [13, 26, 27, 28]. Two bunches with variable separation from a few to many linac RF cycles, less than 1 to hundreds

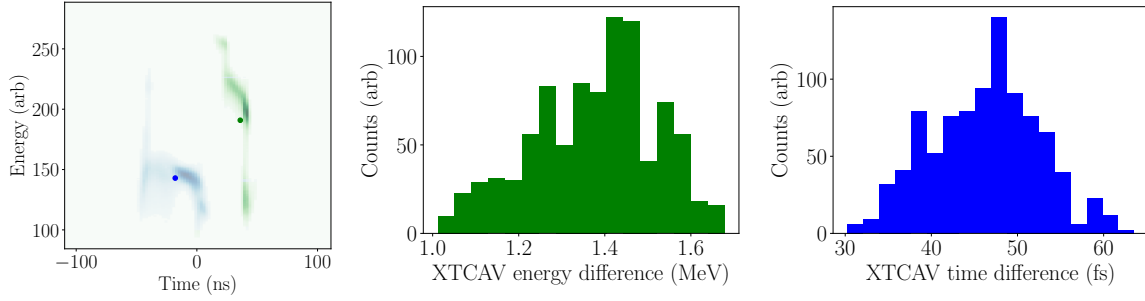


Figure 26: An example of double bunch XTCAV image (left). Energy and time-separation jitter for 50 ns double bunch separation (right). The RMS values are 0.3 MeV and 6.2 fs for energy and time jitter accordingly.

ns, are already available from the two lasers that can drive LCLS copper linac photoinjector.

5.1 Double bunch jitter

LCLS copper linac has repeatedly demonstrated multi-bunch capability for various bunch separations [13, 26, 27, 28]. An important parameter for a successful DBFEL operation is the double bunch time separation jitter. For the first round of measurements, we generated two bunches at about 50 ns or 143 RF-buckets separation, and collected about 1000 XTCAV images. We then analyzed the images, to determine the individual center of mass position of the first and second bunch in both time and energy. This information is used to calculate the RMS jitter in time and energy separation. We found RMS energy jitter to be 0.3 MeV and RMS time jitter to be 6.2 fs respectively; see Fig. 26. We expect the jitter to be significantly smaller for shorter separations. A detailed study is planned shortly after LCLS-II commissioning. Double- and multi-bunch jitter are also critically important parameters for the successful operation of cavity based XFELs [24].

5.2 Photoinjector IR pulse stacking

The current technique for generating two to four bunches with the Cu linac uses pulse stacking in the UV after the IR-to-UV harmonic generators. The multi-bunch generation is more efficiently done by stacking the IR pulses before the Regen Amplifier, Multipass

Amplifier and harmonic generators (Fig. 27). A fast electro-optics switch (EOS) selects a single IR pulse from the modelocked laser oscillator. The gun resonant frequency is 2856 MHz. The fast EOS can select a single laser pulse at a repetition rate up to 119 MHz, the 24th sub-harmonic of the gun frequency.

After being selected by the EOS, each IR laser pulse is then split into two pulses of approximately equal amplitude with the use of a half-wave plate (HWP) and a pair of prism polarizers. Using the HWP allows us to adjust the relative intensity of the two IR pulses by rotating the c-axis of the HWP with respect to the oscillation direction of the laser electric field. Approximately one-half of the IR pulse with p-polarized electric field is transmitted through the polarizers in the straight-through path. The other half of the IR pulse, having s-polarization, is reflected by the first prism polarizer and sent to an optical delay line consisting of a roof prism mounted on a high-precision translation stage that is adjustable to vary the path length of the delayed laser pulse. The straight-through and the delayed IR pulses are recombined in a second prism polarizer so that their paths are again superimposed, but now, one pulse is trailing behind the other by a distance equal to the optical path length difference between the straight-through path and the delay path.

Since this pulse stacking method uses polarizers for splitting and combining laser pulses traversing different paths, the electric fields of the output laser pulses are polarized along two orthogonal directions. In order for both IR pulses to be amplified in the Regen Amplifier which is also polarization dependent as it uses polarizers for injecting the low-power input beam and ejecting the amplified beam, the polarization angles of both laser pulses have to be rotated by 45° before injection into the Regen Amplifiers. This is done with a HWP in front of the prism polarizer that injects one-half of the power in both laser pulses with s-polarization into the top Regen and Multipass Amplifiers. The other half of the IR power with p-polarization is transmitted and traverses another HWP that rotates its polarization by 90° before injection into the bottom Regen and Multipass Amplifiers. We select the optical path lengths of the two amplifier chain such that when the two sets of pulse pairs are combined, they form a train of four laser pulses with variable separation and approximately equal amplitude. We can also correct for small variations in amplitude of the four IR pulses by adjusting the HWP angles and ramping the gain of the Regen Amplifiers. After the

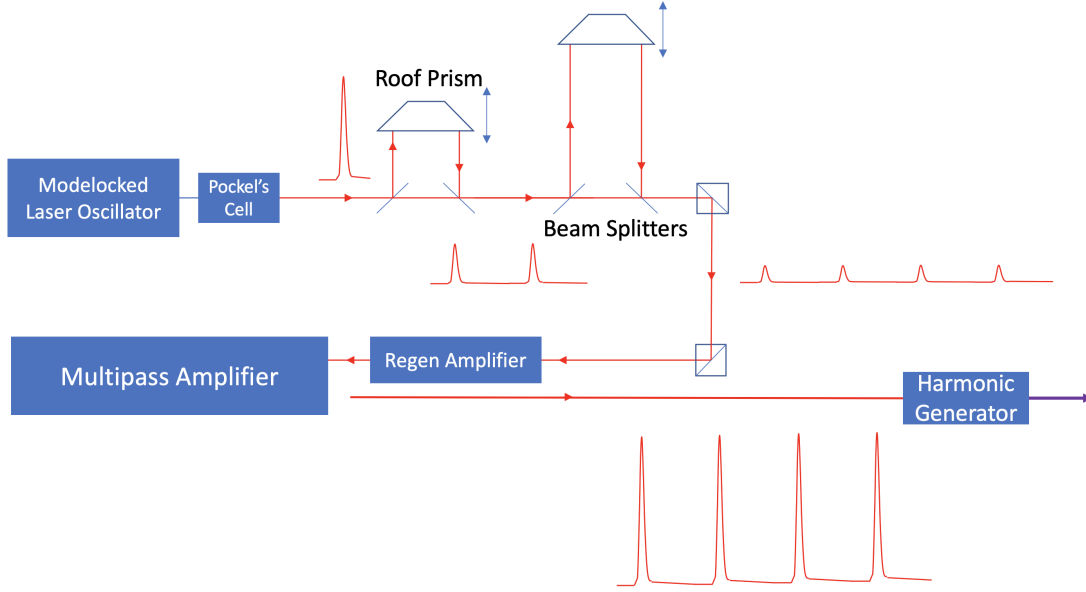


Figure 27: IR pulse stacking schematics: initial IR pulse is doubled and amplified. The process can be repeated to generate four or more high intensity IR pulses, thus mitigating the limit of UV power budget when stacking in UV range.

Regen and Multipass Amplifiers, the high-power IR pulses are converted to UV via two stages of second-harmonic-generation (SHG), with the first stage converting the 760-nm IR into 380-nm (deep blue) light, followed by sum-frequency mixing of these wavelengths to produce the desired 253-nm UV light. We purposely choose to stack the pulses before the two stages of SHG so that any loss of optical power in the pulse stacking process can be compensated for by saturated amplification in the Regen and Multipass Amplifiers. However, pulse stacking with polarization dependent optical elements introduces a complication to the harmonic generation process; that is, the four IR pulses alternate between s-polarization and p-polarization. This complication requires that we use a Type-II phase-matched SHG crystal such as potassium titanyl phosphate (KTP) oriented at 45° angle with respect to both laser polarizations as the first SHG crystal for the IR-to-blue frequency conversion. The frequency conversion from blue to UV can be done with a Type-I phase-matched SHG crystal, such as beta barium borate (BBO).

5.3 Ultra-fast e-beam kicker design

Initially, the first bunch has to propagate on axis in order to provide high power seeding signal. The second bunch has to be put off axis before the SASE section, with large enough offset to suppress its lasing. This will be done with an ultra-fast transverse electromagnetic (TEM) kicker system. The quality of the lasing bunch is defined by the ultra-fast kicker's rise time stability. Overall performance of the DBFEL system is critically dependent on the ability to control the orbits of two bunches. Similar kickers were designed for high energy electron beams, including LCLS-II, albeit at larger bunch separations. In case of DBFEL at LCLS-II, double bunch separation is about 0.7 ns. The transverse kick required to suppress lasing in the undulators is given by $\theta_C = \sqrt{\lambda/L_g}$, where λ is the radiation wavelength and L_g is the gain length [29]. This value is in the order of 10 μ rad and is translated into about

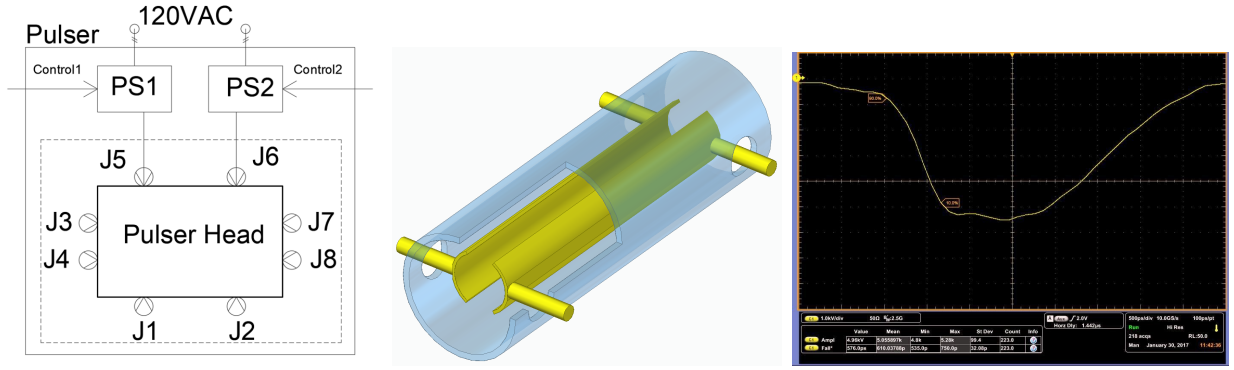


Figure 28: Pulser block diagram (left). J1, J2, ..., and J8 are the pulser head connectors, PS1 and PS2 are the pulser head power AC-DC converters with a controllable DC voltage levels by Control1 and Control2 signals. A schematic view of vertical TEM kicker (middle). Ultra-fast pulser's prototype voltage as a function of time (scale is 0.5 ns/div) (right).

60 keV/c of transverse momentum at 6 GeV beam energy, thereby determining the required TEM kicker strength. For a TEM structure, kicker strength is given by

$$\alpha = \frac{2VL}{r} \frac{4}{\pi} \sin \frac{\psi}{2}, \quad (4)$$

where $\psi = \pi/3$, V is the voltage, L is the length of the TEM structure, r is the structure radius and ψ is the opening angle [30]. Assuming TEM structure length of about 0.1 m with aperture of 0.01 m, we obtain minimum 3 kV of required voltage.

Parameter	Units	Value
Max. voltage	kV	± 10
Tuning range (lower)	kV	-10..-7
Tuning range (upper)	kV	7..10
Rise time	ns	<0.5
Flat top	ns	3.5 ± 0.5
Pre-pulse	-	$<2\%$
Measured voltage range	-	$>95\%$
Impedance	Ohm	50
Rep. rate	Hz	120
Pulse-to-pulse time jitter (RMS)	ps	35
Amplitude jitter	ppm	<50

Table 4: Ultra-fast TEM kicker specifications.

We then consider a TEM structure, as shown in Fig. 28, with the specifications listed in 4. In this configuration, high voltage pulse is applied on two vertical plates, filling up TEM structure with EM field collinear with the beam direction. Our initial experiments with pulser prototypes show promising results for 5 kV peak voltage, 0.7 nsec rise time on a 50 Ohm resistive load; see Fig. 28. Pulser power supply design will be based on an employment of drift step recovery processes in semiconductors.

Successful DBFEL operation requires a high fidelity <0.7 ns high voltage pulser. Ultra-fast pulser will be installed in the accelerator vault, in the "instrument section" at the end of Linac Sectors 21 and 22. It will be shielded with lead blocks and operate at room temperature. We provide a block-diagram of the pulser head in Fig. 28, list of its specifications in Tab. 4 and additional requirements. Pulser head has two independent controlled outputs J1 and J2 (two channels: positive and negative relative to the ground). Output amplitude tuning in the channels is controlled by the value of the DC supply voltages (PS1 and PS2) through the J5 and J6 connectors. The rise time of voltage in each channel J1 and J2 must be less than 0.7 ns (better 0.5 ns) (RMS) in each channel measured at the output voltage

levels from 5% to 95% in the range shown above. Pulser head must be triggered independently by the external TTL standard level trigger through the J3 and J4 connectors, and its stability (a time jitter of the output pulse against the trigger input) must be better than 0.5 ns. Output waveforms in J1 and J3 have a flat part (better than 10%) of the pulse shape with a practically constant amplitude during (3.5 ± 0.5) ns. To ensure final waveform stability, SSDN-414-05 current probes must be integrated in both channels in the pulser head and producing the output signals at J7 and J8 connectors. The current probes have to be installed on the final slow cells of the pulser head (before the components which are used for sub-nanosecond rise time).

6 DBFEL scientific applications

In this sections we consider several modes of operation of the DBFEL system and discuss the new scientific opportunities it opens for the LCLS-II copper linac based FEL. What we present here is not a complete list of all experiments made possible by DBFEL but only a discussion of some of the applications that significantly extend the science at LCLS-II.

DBFEL gives us the possibility of generating X-ray pulses with a power of about 650 GW at 4 keV, with a small linewidth, as discussed before. For a pulse duration of 15 fs, the intensity is 10 mJ, corresponding to about 1.5×10^{13} total 4 keV photons, corresponding to 10^{12} photons/femtosecond. With the K-B mirrors existing in the CXI beam line the X-rays can be focused to about 100 nm spot size, giving a power density at the focal point of 2×10^{21} W/cm⁻². This value can be compared with 10^{22} W/cm², obtainable from the most recent PW laser focused to 1.7 μ m.

The large number of photons is critical for nonlinear scattering and absorption processes which have low cross-sections, like 2-photon inelastic scattering or 2-photon photoionization. DBFEL pulse of 4 keV, when focused to 150 nm, yields a fluence of 8.5×10^6 photons/Angstrom². The large number of photons per fs is important for coherent diffraction imaging and imaging before destruction.

The large power density obtainable focusing the pulse to 100 or better is important for high field science. The power density obtainable at the focus is quite large, 3×10^{21} W/cm²

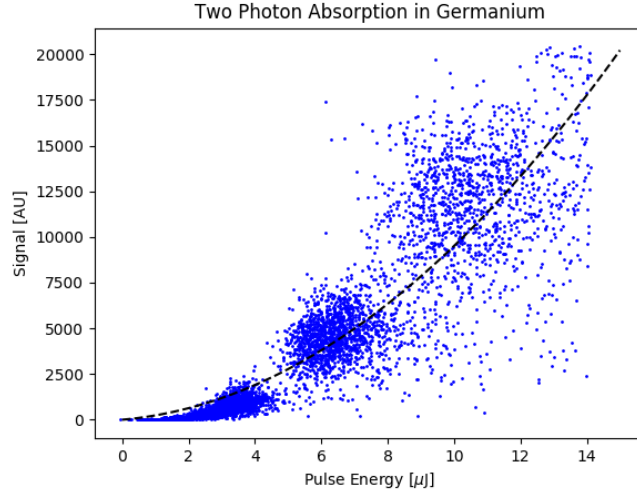


Figure 29: Two-photon photoionization of Germanium

if there are no losses in the KB focusing system. If we assume a 30% loss, as seen from the experimental data, we still have 10^{21} W/cm² a value near to that obtainable focusing a 1PW laser to a 3 micron spot size. The electric field at the focus is about 6×10^{13} V/cm, a value much larger than the atomic electric field, about 5×10^{11} V/m, allowing new studies of non linear atomic physics. As we will discuss later in this section, with some improvements in the K-B focusing system it is possible to focus the X-ray pulse to about 10 nm, raising the power density by a factor of one hundred and the electric field by a factor of ten, further extending the DBFEL scientific exploration area.

6.1 2-photon absorption at 4 keV

DBFEL will enhance the existing experimental measurements as well as enable many new experiments of this kind. For example, one can study K-edge dichroism in iron, nickel and cobalt. Typically this is done with circular L-edge spectroscopy as one looks at P to D transitions (as the 3d orbitals/bands contain the magnetic information for these elements). With two photon absorption one can induce a direct S to D transitions as the selection rules allow it. Fig. 29 illustrates the required fluence, using the CXI 100 nm focus, and signal for two photon absorption process in Germanium.

6.2 High fluence diffractive imaging

In addition to high field physics, high power X-ray pulses are beneficial for holography, coherent diffraction imaging (CDI), and single particle imaging (SPI) [31]. While in SPI there is a tradeoff between the number of collected data frames and the pulse fluence, the technique works just as well with 1/10th of the fluence if 10x more data was collected. However, 2D CDI and holographic methods benefit as they are single shot methods. Increasing the number of photons per pulse by a factor of 100 at 4 keV increases the 2D single shot reconstruction resolution by a factor of 10. This is significant as single shot imaging techniques are limited by shot noise (number of photons in the outer most resolution shell) of the diffraction pattern. Current single shot X-ray hologram resolution is of order 14 nm [32], a factor of 10 increase in resolution places the method into the sub-nm regime. For single particle imaging applications higher fluences reduces the number of required data frames needed for a 3D reconstruction. For a given resolution we note that the number of data frames needed decreases linearly with pulse fluence. Finally, we point out that improvement in 4 keV photon fluence drastically enhances virus imaging [33].

6.3 DBFEL pump-probe two color mode

DBFEL can be operated in two-color configuration, where the first bunch is used to generate a narrow bandwidth seed signal, and second bunch produces a high power SASE pump pulse at a different photon energy, similarly to [34]. To obtain two colors, the second undulator section is tuned to a different value of K . Similar split-undulator configuration, with a channel-cut Si (111) monochromator, is currently employed at SACLA in Japan. An example of two color experiments is the recent work on Mn amplified emission (ASE) where one SASE pulse is used to generate population inversion and the other monochromatized pulse is used to seed the process [35]. Starting from a seed instead of fluorescence noise increases the output power and reduces intensity fluctuations. Pump-probe experiments can also benefit from the increased intensity in the two colors obtained with using two bunches with respect to using two slices of the same bunch or two bunches within the same RF cycle [36, 37]. Therefore the DBFEL experimental infrastructure, when built, would allow many new fundamental

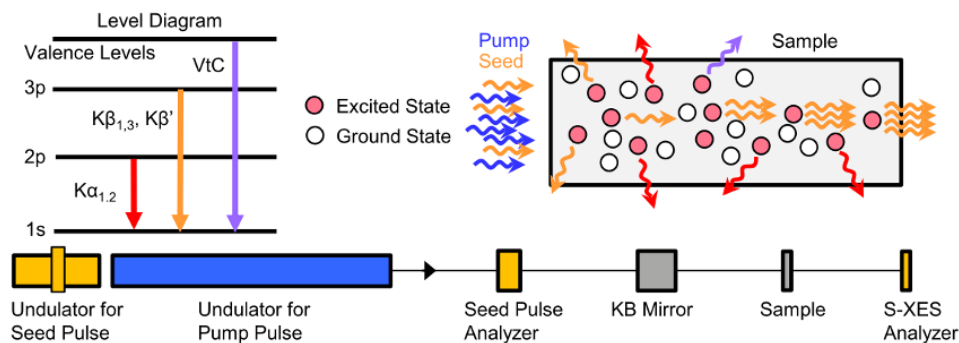


Figure 30: Concept of seeded K_α/K_β S-XES and schematics of experimental setup. Left: Level scheme of different K emission lines following 1s core hole excitation. Right: The pump pulse creates a population inversion of 1s core-hole excited states. The monochromatic seed pulse stimulates the emission of K_α/K_β photons along the seeding direction. (The seeded S-XES is shown here for K_β). Bottom: Schematics of the experimental setup.

physics experiments, extending the research reach of LCLS.

6.3.1 S-XES spectroscopy with two-bunch two-color operation

A molecular level understanding of the function of transition metal complexes has been a grand challenge. Synchrotron radiation (SR) based X-ray spectroscopy methods have been at the center of studying transition metal complexes for many years, specifically as element sensitive probes of their electronic structure and ligand environment. Recently this research has been upgraded to use X-ray free electrons lasers (XFELs), where ultra-short and ultra-bright X-ray pulses have opened the door to investigate ultra-fast phenomena as well as systems beyond the reach of SR based probes [38, 39, 40, 41]. Most studies so far have used the conventional approach of X-ray spectroscopy in the linear regime, where transition metal complexes are typically studied at their L- and K-edges with X-ray absorption or emission spectroscopy (XAS, XES) and resonant inelastic X-ray scattering (RIXS)[42, 43]. Due to the stochastic nature of XFEL pulses, XES in a shot-by-shot approach using the full self-amplified spontaneous emission (SASE) beam for excitation, has been so far the preferred method [38, 39, 41, 44]. However, linear XES has some fundamental limitations mainly due to the large core-hole lifetime broadening and the small spectral sensitivity to

electronic structure changes in the stronger lines ($K_{\alpha 1,2}$, $K_{\beta 1,3}$). This limitation can be partly addressed by measuring the weaker valence-to-core (VtC) lines, providing more detailed chemical information, but hampered by the the very weak signal strengths [42, 45].

The approach we propose here is stimulated XES (S-XES) where a nonlinear X-ray interaction forces a higher shell electron back into the core-hole of the initially excited state. When population inversion is achieved, S-XES will show an exponential gain with the signal emerging mainly collinear with the XFEL beam in the forward direction [46, 47, 35]. S-XES can in principle be used as a spectroscopy tool to study the electronic structure of the Mn absorber. To gain more quantitative understanding of S-XES, we will apply the new two-color capability of DBFEL to create a monochromatic, tunable seed pulse, with a strong pump pulse. Specifically, we propose to study the spectral shape of seeded S-XES from Mn(II)Cl_2 and NaMn(VII)O_4 solutions at various concentrations. In addition to seeded K_α S-XES, we will attempt to seed the weaker but chemically more sensitive K_β line. We have recently been able to observe seeded K_β S-XES using a SASE seed pulse at LCLS. Using the self-seeded monochromatic seed pulse will critically enhance the control and electronic structure sensitivity of two-color seeded S-XES. By tuning the seed pulse through the spectrum of the S-XES signal, we hope to selectively seed spectral features. These experiments will be the crucial next step for developing S-XES into a quantitative spectroscopy tool.

6.3.2 Coherent anti-Stokes Raman spectroscopy at 4 keV

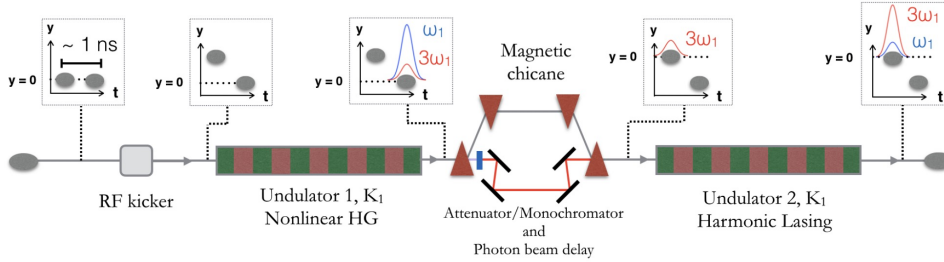
The two color DBFEL mode would also enable significant 4 wave mixing experiments such as coherent anti-Stokes Raman (CARS) spectroscopy or stimulated X-ray Raman scattering. For example, one can investigate low Z elements in condensed systems where resonant scattering is impossible due to the sample thickness. Typically such systems use X-ray Raman scattering, an inelastic X-ray technique. However this method is very slow and can not be used to look at dynamic processes like the dynamics of Lithium in a battery cell.

If we consider the battery experiment we would like to observe a resonance with the Lithium's K-edge energy of $\omega_V = 54.7$ eV. The experiment would produce a strong SASE pump pulse of $\omega_1=4,055$ eV with the second electron bunch, and a narrow-bandwidth probe pulse of $\omega_2=4,000$ eV. We will then observed the stimulated Raman signal, an increase in

the 4,000 eV probe, or the CARS signal at $\omega_{cars} = \omega_1 - \omega_2 + \omega_1 = 4,110$ eV. The tunability of DBFEL monochromator will allow for precise scan of the probe pulse *possibly* making it a valuable tool for spectroscopy, similarly to stimulated Raman case.

6.4 Hard X-ray harmonic lasing

(a) Double bunch harmonic lasing and/or fresh bunch self-seeding



(b) Double bunch harmonic seeding

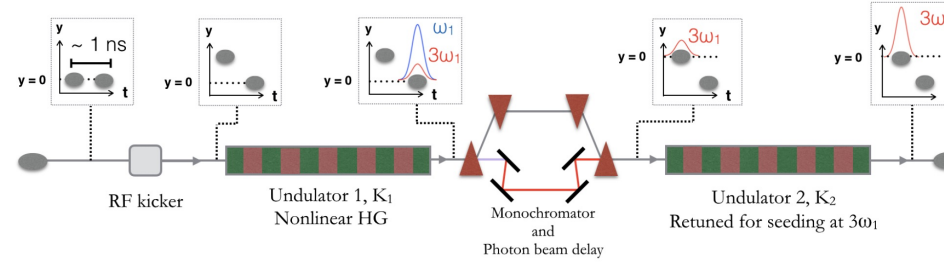


Figure 31: Double-bunch harmonic lasing schematic taken from Ref [6]. The first undulator section generates the fundamental and, through nonlinear harmonic generation, the third harmonic. The radiation is passed through a monochromator and/ or attenuator to transmit the desired harmonic and attenuate the other, and to delay the X-ray pulse to temporally overlap with the second fresh electron bunch.

The DBFEL can also be operated in a harmonic lasing configuration (see Fig 31). Harmonic lasing can be used to extend the wavelength range of the FEL with increased power, spectral brightness and improved stability compared to the (nonlinear) harmonic emission that naturally results from the FEL process. In a single-bunch FEL amplifier, the performance of harmonic lasing schemes is strongly limited by the increased slice energy spread of the lasing electrons. To circumvent this limitation, the DBFEL was proposed as a driver for an efficient and compact harmonic lasing scheme in Ref. [6]. Start-to-end simulations

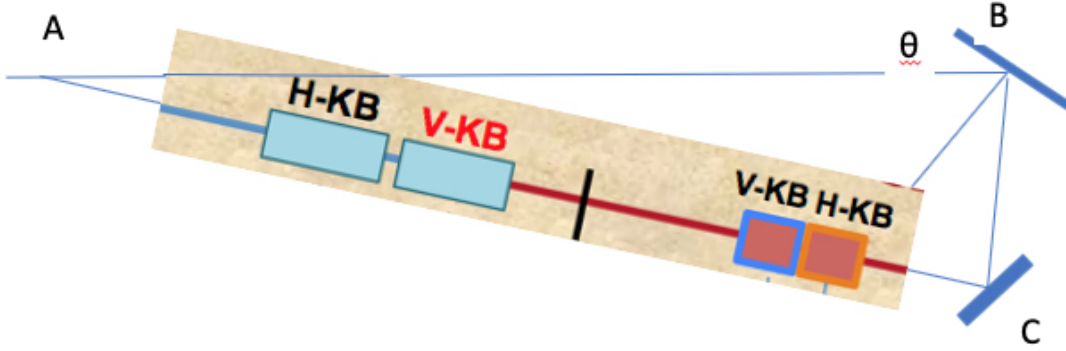


Figure 32: The turning around can be realized with small losses using two diamond crystals with a Bragg angle $> 45^\circ$, bending the photons more than 90° per mirror. This can be done for photons of 4.2 keV and $C^*(1, 1, 1)$ crystals. The KB mirrors for focusing are inserted in the return leg.

for this scheme with an advanced superconducting undulator have shown the feasibility of reaching ~ 10 GW power at a photon energy of 37 keV in a 75 m long undulator. This represents more than an order of magnitude increase in X-ray brightness compared to nonlinear harmonic generation at the same photon energy. The proposed hardware for the DBFEL installation at LCLS would enable harmonic lasing schemes of this type to be tested with the simple addition of an attenuator in the X-ray delay line.

Harmonic lasing can extend the photon energy to over 36 keV, using the present HXR undulator and even more with a new superconducting undulator.

6.5 High Field QED: $e\gamma$ - and $\gamma\gamma$ -colliders

Recent developments in laser technology will open the avenue for previously unseen highly nonlinear regimes of light-light, and particle-light interactions [48, 49]. At SLAC, such experiments are planned at FACET-II facility using the ultra-relativistic electron beam and a high power CO₂ laser. XFELs can also be used to study these phenomena, using high reflectivity crystals to turn around an X-ray pulse by an angle near π as shown in Figure 32.

Colliding TW X-ray pulses with GeV scale electron beam, as shown in see Fig. 33,

the electric field strength in the electron rest frame is multiplied by the factor γ of the transformation from the laboratory frame to the electron rest frame, increasing its a value by many orders of magnitude. To provide even larger electric field, one may further reduce the X-ray spotsize. For example, a 4 keV 1 TW X-ray pulse, focused down to 10 nm spotsize, yields $10^{15}V/m$, a value similar to that obtainable from a PW laser focused to a few micrometers. In the electron rest frame the electric field is about $E = 10^{19}V/m$, larger than the Schwinger critical field ($1.32 \times 10^{18}V/m$).

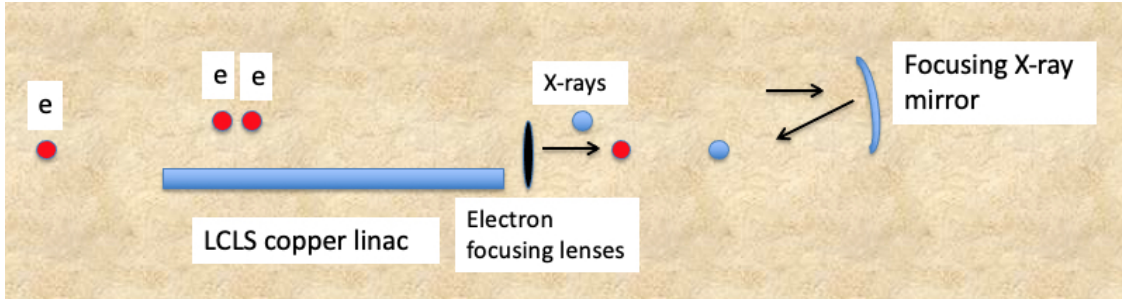


Figure 33: The first two electron bunches generate a high power X-ray pulse which, after being reflected back and focused, interacts with the third electron bunch. An additional electron focusing lens is used to reduce the electron beam radius at the collision point. The third bunch delay is about one hundred nanosecond.

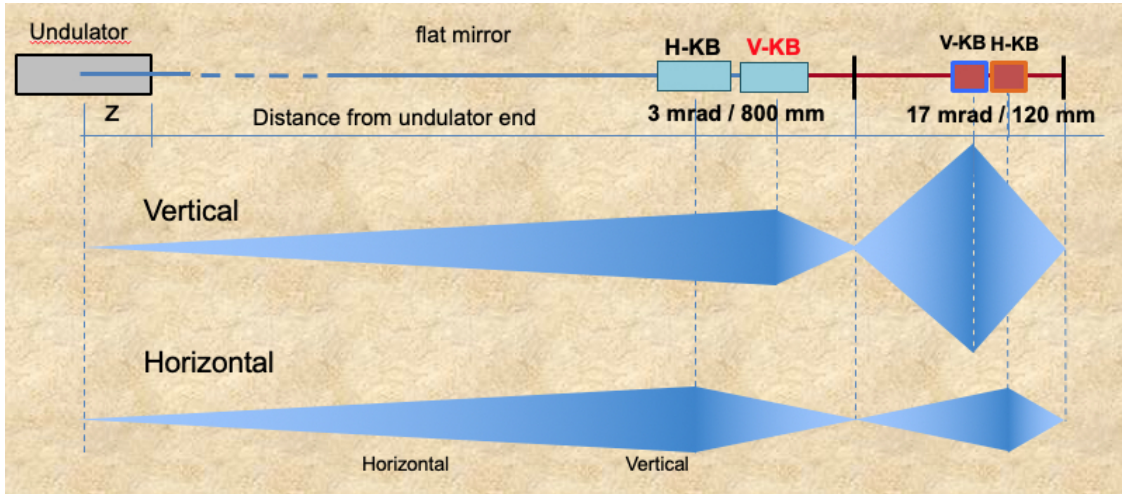


Figure 34: Four KB mirrors, two horizontal and two vertical, are used to focus to a near 10 nm spot size.

Recently X-ray focusing capabilities to single nm scale have been extensively explored at SACLA using KB-mirrors [50, 51]. We envision this technique will be extended to high power X-ray pulses in the near future, making the experiment discussed feasible. An example of focusing to small spot size, using four KB mirrors in a double focusing configuration, is shown in Fig. 34 and the results of propagating the X-ray pulse to the focal point are shown in Fig. 35. With this focusing system we obtain a spot size of 11.7×12.5 nm FWHM, including reflectivity and elongation effects, and $5 \times 10^{23} \text{W}/\text{cm}^2$ for a 1 TW X-ray pulse. The required mirror polishing is about 1 nm, within present polishing and metrology limits. Using this system DBFEL offers a unique opportunity to probe electron-photon interaction in a regime with the field larger than the Schwinger limit and normalized vector potential smaller than one, a regime not accessible using visible PW lasers, as shown in Fig. 36.

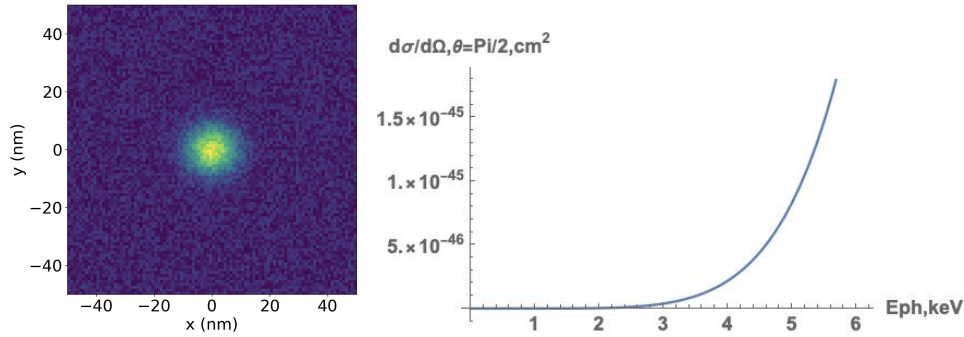


Figure 35: Left: X-ray spot of 11.7×12.5 nm FWHM at the focal point. Right: photon-photon scattering cross-section as a function of photon energy.

Another interesting possibility is observing photon-photon scattering. The cross section for this process is given by:

$$\frac{d\sigma}{d\Omega} = \frac{139\alpha^4\omega^6}{(180\pi^2)m^8}(3 + \cos^2\theta)^2 \quad (5)$$

The cross section has a strong dependence on photon energy, growing like the sixth power of the photon energy, giving a big advantage to X-rays over visible photons; see Fig. 35. In a head-on collision between the two photon beams the geometry is that of a photon-photon collider, and the luminosity is given by:

$$L(P, \sigma, E_{ph}) = f * (PT_{pulse}/(eE_{ph}))^2/(\pi * \sigma^2)$$

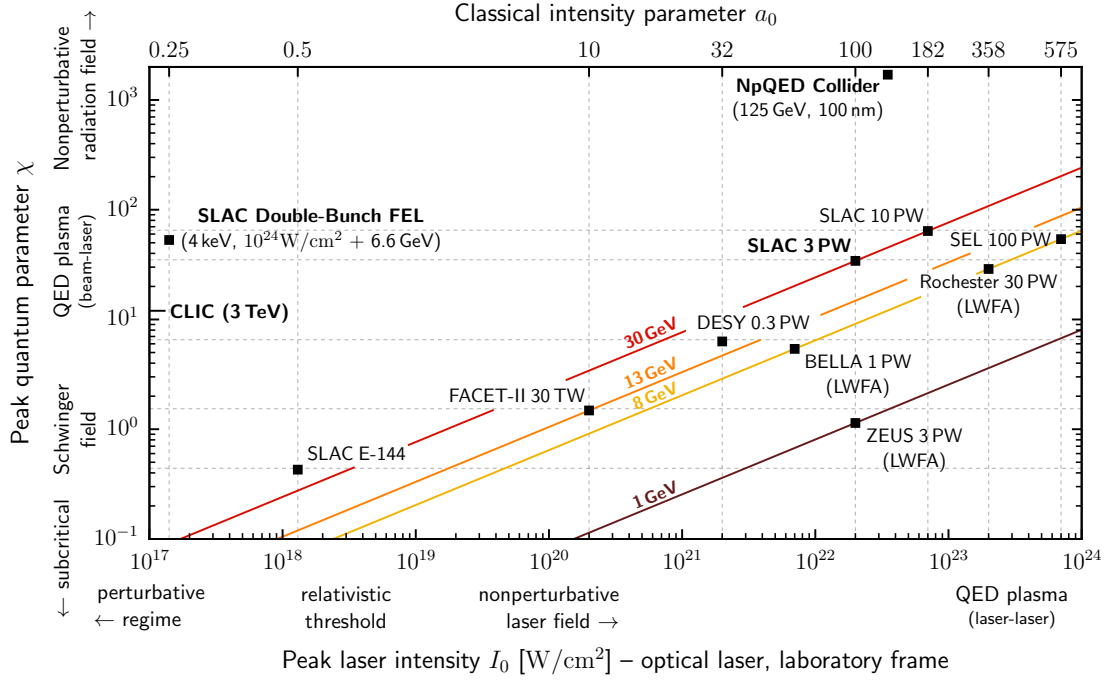


Figure 36: A summary plot of possible future QED collider projects in χ - a_0 parameter space.

where e is the electron charge, the photon energy is in eV, T_p is the pulse duration and f the pulse repetition rate. At 7 keV, the maximum photon energy allowed by the present DBFEL configuration, 300 GW power and a collision cross-section of 100 nm we have $L = 5 \cdot 10^{36}$ /cm². For a total cross-section of $1.0 \cdot 10^{-43}$ cm⁻² we would have about 0.03 events per day, using the LCLS repetition rate of 120 Hz. The number grows to 3 events/day at $\sigma = 10$ nm. The number of events grows rapidly with the photon energy, making this experiment more attractive. Using the AGU undulator would also give a large boost to the event rate.

6.6 XFEL enhanced nuclear fusion cross-sections

Recent upgrades at the Linac Coherent Light Source (LCLS) will allow the testing of theories that predict increased quantum-mechanical tunneling probabilities of nuclear fusion reactions [52, 53]. These capabilities together with possible near-future upgrades such as the Double Bunch X-ray Free Electron Laser (DBXFEL) are poised to demonstrate electric field-assisted nuclear fusion enhancements and to determine the dependence on the electric field strength and frequency. The present LCLS X-ray beam already delivers X-ray intensities of 2×10^{20} W

cm^{-2} at 10 keV photon energies thus exceeding electric field strength values of $E_{XFEL} = 10^{13} \text{ V/m}$ for which dynamical nuclear fusion assistance has been predicted to occur [52]. A future DBXFEL mode of operations will further allow increases in the electric field strength by a factor of 20 due to the higher photon flux and improved X-ray focus from the present 100 nm spot to a future 10 nm spot. These capabilities will thus open up detailed future studies of nuclear fusion cross section enhancements. Finally, a dedicated undulator and possible improvements in beam quality suggest future XFEL intensities of $10^{24} \text{ W cm}^{-2}$ producing field strengths well above $E_{XFEL} = 10^{15} \text{ V/m}$ directly deforming the nuclear potential barrier and affecting the tunneling probability.

All concepts for Inertial Fusion Energy (IFE) rely on hot spot formation and assembly of nuclear fuel. Within this approach, nuclear fusion reactions are first initiated within the hot spot volume producing fusion yield and energetic fusion reaction nuclei that stop and deposit their kinetic energy within the cold and dense nuclear fuel. At sufficiently large fusion reactivities and densities, simulations show that a nuclear burn wave will be launched into the nuclear fuel burning significant fractions and resulting into net energy gain.

In the most advanced schemes presently pursued within the Inertial Confinement Fusion (ICF) approach to ignition, a hot spot forms in the center of a spherical implosion surrounded by deuterium-tritium fuel that is compressed near an isentropic implosion trajectory reaching ion densities of $N_i = 10^{26} \text{ cm}^{-3}$. Recent experiments on the National Ignition Facility (NIF) have converted $> 5 \%$ of the driver energy into fusion energy [54]. In addition, alternative fast ignition concepts are being pursued that use high-power short-pulse lasers or laser-produced proton beams to produce a hot spot in near isobarically compressed matter [55].

Consequently, bringing enhanced fusion cross sections to inertial fusion energy research can open up the field to more advantageous hot spot formation physics and has the potential to pave the way for future advances using smaller fusion drivers or the usage of advanced fusion fuels. The latter is particularly attractive if the need of radioactive nuclear fuel, i.e., tritium, and the requirements for breeding can be avoided.

One of the early successes of quantum mechanics was Gamow's derivation of the α -decay rate [56] via tunneling of the α -particle through the nuclear potential and thus explaining the Geiger-Nuttall law [57]. Building on this result we can evaluate tunneling in the inverse

direction arriving at the familiar expression for the nuclear fusion cross section

$$\sigma(\epsilon) = \frac{S(\epsilon)}{\epsilon} \exp(-\sqrt{\epsilon_G/\epsilon}), \quad (6)$$

with ϵ being the center-of-mass energy, S the slowly varying astrophysical S -factor, and $\epsilon_G = (\pi\alpha_f Z_1 Z_2)^2 2m_r c^2$ the Gamow energy. Here, α_f is the fine structure constant, m_r is the reduced mass of the two fusion nuclei, and c is the speed of light.

Theory suggests that the addition of a dynamical time-varying electric field can drastically enhance the tunneling probability. The barrier transparency \mathcal{T} in Eq (6) will need to be replaced via:

$$\mathcal{T} = \exp(-\sqrt{\epsilon_G/\epsilon}) \rightarrow \exp(-\sqrt{\epsilon_G/(\epsilon + h\nu)}). \quad (7)$$

In Ref. [52], for $\epsilon = 1$ keV and an X-ray laser energy of 10 keV, the authors estimate an enhancement factor of 10 orders of magnitude. Obviously, higher X-ray energies are already available at X-ray laser facilities. Although DBXFEL pulses are relatively short and predicted to deliver 15 fs long pulses at ≤ 10 keV it is important to scale to higher photon energies to deliver a field whose time variation is of the order of the tunneling time; in this case, tunneling enhancements have been predicted for $E_{XFEL} = 10^{13}$ V/m [58].

Directly observing nuclear fusion enhancements will require the use of a dense target that delivers hydrogen isotopes to the XFEL focus. Cryogenic deuterium jets [59, 60] and room-temperature heavy water jets [61, 62] have recently been successfully fielded in laser and XFEL facilities. They have the advantage to allow experiments at high repetition rates and have already demonstrated predictable neutron yields in short-pulse laser facilities. Experiments suggest neutron production rates of 10^6 neutrons/joule [63, 64]; thus, using a 100 mJ short pulse laser to heat the target to 1 keV temperatures suggests a thermal background signal of 10^5 neutrons. Further, assuming a $5\mu\text{m}$ cylindrical jet at liquid densities of $5 \times 10^{22} \text{ cm}^{-3}$ and an XFEL spot of 100 nm provides a volume of $V = 5 \times 10^{-14} \text{ cm}^{-3}$ and a maximum number of 10^9 fusion reactions that are easily detectable. In the same geometry, a 10 nm XFEL focus would allow 10^7 fusion reactions, again easily detectable.

A detailed experimental test of fusion cross section enhancements will include the following studies:

1. Perform absolute neutron yield measurements and quantify the tunneling enhancement

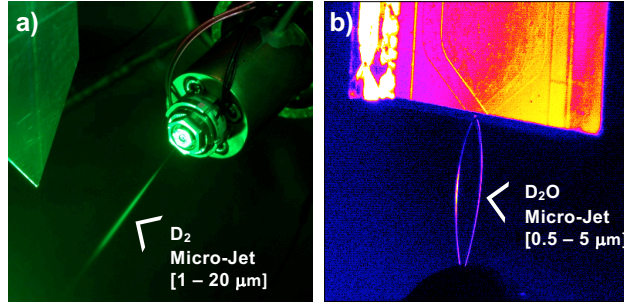


Figure 37: Examples of jet targets suitable for testing tunneling enhancement in heavy hydrogen isotopes at X-ray Free Electron Lasers. (left) A cryogenic deuterium jet has been demonstrated at 120 Hz in LCLS experiments with a target thickness in the range of $1\mu\text{m}$ to $20\mu\text{m}$. (Right) Room temperature heavy water jets have been demonstrated at 380 Hz in LCLS experiments with a target thickness in the range of $0.5\mu\text{m}$ to $5\mu\text{m}$.

by comparing experiments with and without the field of the XFEL. These studies will need to provide data to estimate the pre-factor in Eq. 6 in the presence of the electric field of the XFEL.

2. Perform measurements by scaling the electric field of the XFEL by varying the total photon flux and focusing; attempt to assess the regime of direct potential deformation.
3. Perform measurements by tuning the photon energy to validate the scaling laws for dynamical assistance. Here, the advantage of tune-ability of XFELs and future increases of the photon energy to 25 keV (planned for 2021 at LCLS) and potentially up to 70 keV in the longer term can provide significant insight into tunneling processes.

References

- [1] G. Geloni, V. Kocharyan, and E. Saldin. Scheme for generation of highly monochromatic X-rays from a baseline XFEL undulator. *arXiv*, 2010.
- [2] G. Geloni, V. Kocharyan, and E. Saldin. Extension of self-seeding scheme with single crystal monochromator to lower energy < 5 keV as a way to generate multi-TW scale pulses at the European XFEL. 2012.
- [3] Y. Ding, Z. Huang, and R. D. Ruth. Two-bunch self-seeding for narrow-bandwidth hard x-ray free-electron lasers. *Phys. Rev. ST Accel. Beams*, 13:060703, Jun 2010.
- [4] A. Halavanau, F.-J. Decker, C. Emma, J. Sheppard, and C. Pellegrini. Very high brightness and power LCLS-II hard X-ray pulses. *Journal of Synchrotron Radiation*, 26(3), May 2019.
- [5] A. Halavanau, F.-J. Decker, Y. Ding, C. Emma, Z. Huang, J. Krzywinski, A. Lutman, G. Marcus, C. Pellegrini, and D. Zhu. Generation of High Peak Power Hard X-Rays at LCLS-II with Double Bunch Self-seeding. In *Proceedings, 10th International Particle Accelerator Conference (IPAC2019): Melbourne, Australia, May 19-24, 2019*, page TUPRB088, 2019.
- [6] C. Emma, Y. Feng, D. C. Nguyen, A. Ratti, and C. Pellegrini. Compact double bunch x-ray free electron lasers for fresh bunch self-see and harmonic lasing. *Phys. Rev. Acc. and Beams*, 20:030701–10, 2017.
- [7] C. Emma, A. Lutman, M. W. Guetg, J. Krzywinski, A. Marinelli, J. Wu, and C. Pellegrini. Experimental demonstration of fresh bunch self-seeding in an x-ray free electron laser. *Applied Physics Letters*, 110(15):154101, 2017.
- [8] J. Qiang, S. Lidia, R.D. Ryne, and C. Limborg-Deprey. Three-dimensional quasistatic model for high brightness beam dynamics simulation. *Phys. Rev. ST Accel. Beams*, 9:044204, 2006. [Erratum: *Phys.Rev.ST Accel.Beams* 10, 129901 (2007)].

- [9] M. Borland. elegant: A Flexible SDDS-Compliant Code for Accelerator Simulation. In *6th International Computational Accelerator Physics Conference (ICAP 2000) Darmstadt, Germany, September 11-14, 2000*, 2000.
- [10] S. Reiche. GENESIS 1.3: a fully 3D time-dependent FEL simulation code. *Nuclear Instruments and Methods in Physics Research A*, 429:243–248, June 1999.
- [11] C. Mayes and A. Halavanau. lume-genesis package. <https://github.com/slaclab/lume-genesis>.
- [12] C. Mayes. lume-impact package. <https://github.com/ChristopherMayes/lume-impact>.
- [13] F. J. Decker et al. A demonstration of multi-bunch operation in the LCLS. In *Proceedings of FEL2010, Malmoe, Sweden*, page 467, 2010.
- [14] K Bane. Wakefield calculations for the lcls in multibunch operation. *SLAC-PUB-16039*, 10 2011.
- [15] J. Wu and et al. Multi-dimensional optimization of a terawatt seeded tapered free electron laser with a multi-objective genetic algorithm. *Nuclear Instruments and Methods in Physics Research Section A: Accelerators, Spectrometers, Detectors and Associated Equipment*, 846:56 – 63, 2017.
- [16] C. Yang, C.-Y. Tsai, G. Zhou, X. Wang, Y. Hong, E. Dong Krug, A. Li, H. Deng, D. He, and J. Wu. The detuning effect of crystal monochromator in self-seeding and oscillator free electron laser. *Opt. Express*, 27(9):13229–13239, Apr 2019.
- [17] C.-Y. Tsai, C. Emma, J. Wu, M. Yoon, X. Wang, C. Yang, and G. Zhou. Area-preserving scheme for efficiency enhancement in single-pass tapered free electron lasers. *Nuclear Instruments and Methods in Physics Research Section A: Accelerators, Spectrometers, Detectors and Associated Equipment*, 913:107 – 119, 2019.
- [18] C.-Y. Tsai, J. Wu, C. Yang, M. Yoon, and G. Zhou. Single-pass high-gain tapered free-electron laser with transverse diffraction in the postsaturation regime. *Phys. Rev. Accel. Beams*, 21:060702, Jun 2018.

- [19] G. Zhou, F.-J. Decker, Y. Ding, Y. Jiao, A. A. Lutman, T. J. Maxwell, T. O. Raubenheimer, J. Wang, A. J. Holman, C.-Y. Tsai, J. Y. Wu, W. Wu, C. Yang, M. Yoon, and J. Wu. Attosecond coherence time characterization in hard x-ray free-electron laser. *Scientific Reports*, 10(1):5961, Apr 2020.
- [20] M. W. Guetg, A. A. Lutman, Y. Ding, T. J. Maxwell, F.-J. Decker, U. Bergmann, and Z. Huang. Generation of high-power high-intensity short x-ray free-electron-laser pulses. *Phys. Rev. Lett.*, 120:014801, Jan 2018.
- [21] C. Emma, K. Fang, J. Wu, and C. Pellegrini. High efficiency, multiterawatt x-ray free electron lasers. *Phys. Rev. Accel. Beams*, 19:020705, Feb 2016.
- [22] H. P. Freund and P. J. M. van der Slot. Studies of a terawatt x-ray free-electron laser. *New Journal of Physics*, 20(7):073017, jul 2018.
- [23] S. Hayama, *et al*, The scanning four-bounce monochromator for beamline i20 at the diamond light source. *Journal of synchrotron radiation*, 25(Pt 5):1556–1564, Sep 2018.
- [24] G. Marcus. RAFEL LCLS-II. In *Proceedings of FEL19*, page TUPRB086, 2019.
- [25] Manuel Sanchez del Rio and Roger J. Dejus. Xop v2.4: recent developments of the x-ray optics software toolkit. *Proc.SPIE*, 8141:8141 – 8141 – 5, 2011.
- [26] F.-J. Decker, *et al*, Two Bunches with ns-Separation with LCLS. In *Proceedings, 37th International Free Electron Laser Conference (FEL 2015): Daejeon, Korea, August 23-28, 2015*, page WEP023, 2015.
- [27] F.-J. Decker, K. Bane, W. Colcho, A. Lutman, and J. Sheppard. Recent Developments and Plans for Two Bunch Operation with up to 1 us Separation at LCLS. In *Proceedings, 38th International Free Electron Laser Conference, FEL2017*, page TUP023, 2018.
- [28] F.-J. Decker, *et al*, Four X-ray Pulses within 10 ns at LCLS. In *Proceedings, 10th International Particle Accelerator Conference (IPAC2019): Melbourne, Australia, May 19-24, 2019*, page TUPRB086, 2019.

- [29] T Tanaka, H Kitamura, and T Shintake. Consideration on the bpm alignment tolerance in x-ray fels. *Nuclear Instruments and Methods in Physics Research Section A: Accelerators, Spectrometers, Detectors and Associated Equipment*, 528(1):172 – 178, 2004. Proceedings of the 25th International Free Electron Laser Conference, and the 10th FEL Users Workshop.
- [30] D. A. Goldberg and G. R. Lambertson. Dynamic devices. a primer on pickups and kickers. *AIP Conference Proceedings*, 249(1):537–600, 1992.
- [31] A. Aquila, *et al*, The linac coherent light source single particle imaging road map. *Structural Dynamics*, 2(4):041701, 2015.
- [32] T. Gorkhover, *et al*, Femtosecond x-ray fourier holography imaging of free-flying nanoparticles. *Nature Photonics*, 12(3):150–153, 2018.
- [33] A. Meents and M.O. Wiedorn. Virus structures by x-ray free-electron lasers. *Annual Review of Virology*, 6(1):161–176, 2019. PMID: 31567066.
- [34] T. Hara, *et al*, Two-colour hard x-ray free-electron laser with wide tunability. *Nature Communications*, 4(1):2919, 2013.
- [35] T. Kroll and et. al. Stimulated x-ray emission spectroscopy in transition metal complexes. *Phys. Rev. Lett.*, 120:133203, Mar 2018.
- [36] A. A. Lutman, *et al*, Fresh-slice multicolour x-ray free-electron lasers. *Nat Photon*, 10(11):745–750, Nov 2016.
- [37] A. Marinelli, *et al*, High-intensity double-pulse x-ray free-electron laser. *Nature Communications*, 6, Jan 2015.
- [38] R. Alonso-Mori, *et al*, Energy-dispersive x-ray emission spectroscopy using an x-ray free-electron laser in a shot-by-shot mode. *Proceedings of the National Academy of Sciences*, 109(47):19103–19107, 2012.
- [39] J. Kern, *et al*, Simultaneous femtosecond x-ray spectroscopy and diffraction of photo-system ii at room temperature. *Science*, 340(6131):491–495, 2013.

- [40] R. Mitzner, *et al*, L-edge x-ray absorption spectroscopy of dilute systems relevant to metalloproteins using an x-ray free-electron laser. *The Journal of Physical Chemistry Letters*, 4(21):3641–3647, Nov 2013.
- [41] W. Zhang, *et al*, Tracking excited-state charge and spin dynamics in iron coordination complexes. *Nature*, 509(7500):345–348, 2014.
- [42] High resolution 1s core hole x-ray spectroscopy in 3d transition metal complexes—electronic and structural information. *Coordination Chemistry Reviews*, 249(1):65 – 95, 2005. Synchrotron Radiation in Inorganic and Bioinorganic Chemistry.
- [43] Ph. Wernet, *et al*, Orbital-specific mapping of the ligand exchange dynamics of $\text{Fe}(\text{CO})_5$ in solution. *Nature*, 520(7545):78–81, 2015.
- [44] Jan Kern, *et al*, Taking snapshots of photosynthetic water oxidation using femtosecond x-ray diffraction and spectroscopy. *Nature Communications*, 5(1):4371, 2014.
- [45] C. J. Pollock and S. DeBeer. Valence-to-core x-ray emission spectroscopy: A sensitive probe of the nature of a bound ligand. *Journal of the American Chemical Society*, 133(14):5594–5601, Apr 2011.
- [46] N. Rohringer, *et al*, Atomic inner-shell x-ray laser at 1.46 nanometres pumped by an x-ray free-electron laser. *Nature*, 481:488 EP –, Jan 2012.
- [47] H. Yoneda, *et al*, Atomic inner-shell laser at 1.5-Angstrom wavelength pumped by an x-ray free-electron laser. *Nature*, 524:446–449, 08 2015.
- [48] G. A. Mourou, T. Tajima, and S. V. Bulanov. Optics in the relativistic regime. *Rev. Mod. Phys.*, 78:309–371, Apr 2006.
- [49] M. Marklund and P. K. Shukla. Nonlinear collective effects in photon-photon and photon-plasma interactions. *Rev. Mod. Phys.*, 78:591–640, May 2006.
- [50] H. Mimura, *et al*, Breaking the 10nm barrier in hard-X-ray focusing. *Nature Physics*, 6:122–125, February 2010.

- [51] K. Yamauchi, *et al*, Single-nanometer focusing of hard x-rays by kirkpatrick-baez mirrors. *Journal of Physics: Condensed Matter*, 23(39):394206, 2011.
- [52] Dynamically assisted nuclear fusion, Friedemann Queisser and Ralf Schützhold, *Phys. Rev. C* **100**, 041601(R) (2019).
- [53] Can Extreme Electromagnetic Fields Accelerate the α Decay of Nuclei? Adriana Pálffy and Sergey V. Popruzhenko, *Phys. Rev. Lett.* **124**, 212505 (2020).
- [54] Update on Laser Indirect Drive Ignition on the National Ignition Facility, M. C. Herrmann, FUSION POWER ASSOCIATES 41ST ANNUAL MEETING, December 16-17, 2020
- [55] The physics of inertial fusion: beam plasma interaction, hydrodynamics, hot dense matter. Atzeni, S.; Meyer-ter-Vehn, J. (2004). Oxford: Clarendon Press.
- [56] Zur Quantentheorie des Atomkernes, G. Gamow, *Z. Phys.* **51**, 204 (1928).
- [57] The ranges of the α particles from various radioactive substances and a relation between range and period of transformation, H. Geiger and J. M. Nuttall, *Philos. Mag. Ser. 6* **22**, 613 (1911); **23**, 439(E) (1912).
- [58] It is interesting to note that S. Ichimaru has predicted a regime called "supernova on the earth" where a dense metallic hydrogen plasma provides favorable conditions for tunneling enhancement close to room temperatures. *Statistical Physics of Dense Plasmas, Elementary Processes and Phase Transitions*, by Setsuo Ichimaru (Taylor and Francis Group 2019).
- [59] Development of a cryogenic hydrogen microjet for high-intensity, high-repetition rate experiments, J. B. Kim, S. Göde, and S. H. Glenzer, *Review of Scientific Instruments* **87**, 11E328 (2016),
- [60] Cryogenic Liquid Jets for High Repetition Rate Discovery Science, Chandra B. Curry, Christopher Schoenwaelder, Sebastian Goede, Jongjin B. Kim, Martin Rehwald,

- Franziska Treffert, Karl Zeil, Siegfried H. Glenzer, Maxence Gauthier, JOVE, doi: 10.3791/61130 (2020).
- [61] Generation and characterization of ultrathin free-flowing liquid sheets, Jake D. Koralek, Jongjin B. Kim, Petr Brůža, Chandra B. Curry, Zhijiang Chen, Hans A. Bechtel, Amy A. Cordones, Philipp Sperling, Sven Toleikis, Jan F. Kern, Stefan P. Moeller, Siegfried H. Glenzer and Daniel P. DePonte, *Nature Communications* **9**, 1353 (2018).
- [62] Structure of heavy water heated by ultrafast laser irradiation at 266 nm, M. Mo *et al.*, *private communications*, (2020).
- [63] Micro-scale fusion in dense relativistic nanowire array plasmas, A. Curtis, C. Calvi, J. Tinsley, R. Hollinger, V. Kaymak, A. Pukhov, S. Wang, A. Rockwood, Yong Wang, Vyacheslav N. Shlyaptsev and Jorge J. Rocca, *Nature Communications* **9**, 1077 (2018).
- [64] Laser neutrons from petawatt laser interactions with cryogenic hydrogen micro-jets, F. Treffert *et al.*, *private communications*, (2021).